LITHOS 398–399 (2021) 106252

Contents lists available at ScienceDirect

LITHOS

journal homepage: www.elsevier.com/locate/lithos

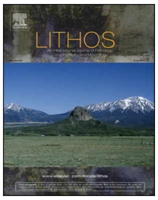

Research Article

A continental forearc serpentinite diapir with deep origins: Elemental signatures of a mantle wedge protolith and slab-derived fluids at New Idria, California

Codi Lazar[a,*], Emily H.G. Cooperdock[b], Bryan H.T. Seymour[a]

[a] Department of Geological Sciences, California State University, San Bernardino, CA, USA
[b] Department of Earth Sciences, University of Southern California, Los Angeles, CA, USA

ABSTRACT

The New Idria serpentinite body in central California has been interpreted as a diapir that was hydrated at depth in the forearc mantle wedge by aqueous fluids released from the subducted slab. This interpretation is primarily based on structural relationships and petrographic analyses of high-grade metabasaltic tectonic blocks entrained within the serpentinite. The geochemistry of the New Idria serpentinites is largely unknown other than a few boron isotope analyses that are consistent with slab-derived fluid compositions, but not definitive. In this contribution, we present whole-rock elemental analyses and petrographic examinations of a suite of ten serpentinite samples to constrain the tectonic origin of the New Idria serpentinite body. Major, minor, and trace element relationships reflect the signatures of depleted peridotitic protoliths typically associated with serpentinites from mantle wedge settings. These include high MgO/SiO_2 vs. low Al_2O_3/SiO_2, high MgO vs. low TiO_2, Cr-rich chromites, and enriched Zr/Nb and Hf/Nb ratios. Unlike in abyssal serpentinites, U is not fluid-mobile and is strongly coupled to Th, with a U-Th relationship that is best explained by melt–rock interaction. Rare earth element fractionation trends are also consistent with melt-rock interaction. Fluid-mobile element (FME) concentrations (Cs, Ba, and Rb) are consistent with a slab-derived signature and are notably enriched, featuring some of the highest Cs and Ba concentrations ever reported in serpentinites. No petrographic or geochemical evidence was found to suggest that these enriched FME signatures resulted from systematic post-serpentinization fluid-rock processes or pre-serpentinization melt-rock interactions. In aggregate, the geochemical signatures of the New Idria serpentinites suggest a highly depleted mantle wedge protolith overprinted by melt-rock interactions and subsequent serpentinization by a slab-derived fluid, consistent with the forearc diapir hypothesis. Although subduction at New Idria ended around 25 Ma, geophysical evidence and simple geodynamic calculations suggest that the timing of the proposed diapiric rise plausibly coincides with the final stages of subduction in central California.

1. Introduction: the New Idria serpentinite body

Serpentinites are abundant along the western margin of North America, emplaced by a variety of tectonic processes related to ongoing and historical subduction. Some of the proposed emplacement mechanisms include obduction from the abyssal seafloor (Barnes et al., 2013) or from a supra-subduction zone (Le Roux et al., 2014), entrainment in accretionary mélange (Shervais et al., 2011), or tectonic accretion of fragmental terranes, as in the Klamath Mountains (Snoke and Barnes, 2006). Another style of emplacement is the buoyant rise of serpentinite diapirs, proposed to have occurred in isolated localities throughout California (Ernst, 2016; Uno and Kirby, 2019; Wakabayashi, 2015, 2017).

The largest of these proposed diapirs is the New Idria serpentinite body (hereafter referred to as "New Idria"), a massif in the Diablo Range of central California (Fig. 1). A diapiric emplacement model for New Idria is supported by several lines of structural evidence. The massif forms the core of an anticline flanked by steeply dipping layers of the neighboring Franciscan and Great Valley Group assemblages, all structurally consistent with an upwarped bulge of rising serpentinite (Coleman, 1961) (Fig. 2). Most of the exposed serpentinite is highly sheared and disaggregated, which is rheologically compatible with the mechanics of low-temperature solid-state diapiric flow (Cowan and Mansfield, 1970). The earliest evidence for subaerial exposure of New Idria is detrital serpentinite debris within the Miocene Big Blue Formation, followed by continuous deposition in the younger San Joaquin Basin and Vallecitos synform (Coleman, 1996). Uplift appears to remain active today, as interpreted from geomorphologic analyses of recent debris flows and observations of detrital serpentinite deposition on marine terraces as young as 500 years old (Atwater et al., 1990; Coleman, 1996; Cowan and Mansfield, 1970).

Although most agree that the basic structure of New Idria is an active serpentinite diapir, opinions diverge regarding its metamorphic origin. Perhaps the most widely accepted hypothesis is that New Idria was

---

* Corresponding author at: 5500 University Pkwy, San Bernardino, CA 92407, USA.
E-mail address: clazar@csusb.edu (C. Lazar).

https://doi.org/10.1016/j.lithos.2021.106252
Received 1 November 2020; Received in revised form 21 April 2021; Accepted 22 May 2021

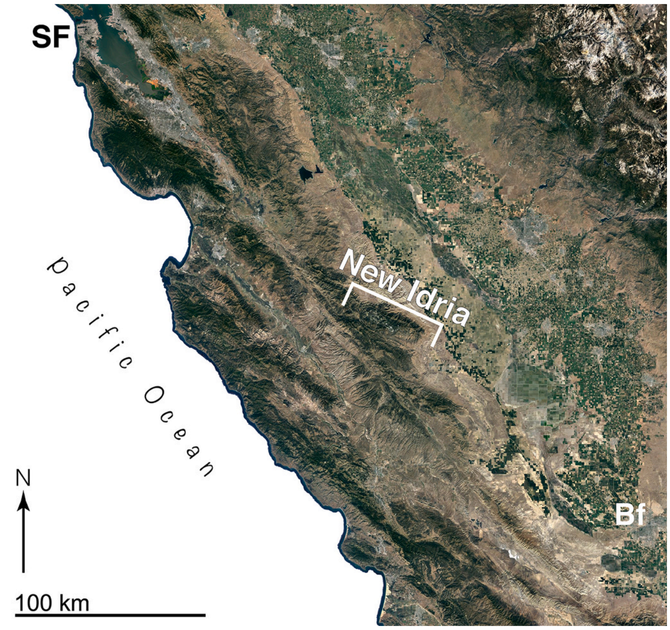

Fig. 1. Satellite image of the New Idria serpentinite body, central California. SF = San Francisco; Bf = Bakersfield.

initially serpentinized in the forearc mantle wedge by fluids expelled from the subducted Farallon Plate. Indirect evidence for this deep source hypothesis is provided by petrographic analyses of an isolated outcrop of high-grade tectonic metabasalts entrained in the serpentinite body, which includes retrograded eclogites, blueschists, and jadeitites, collectively yielding equilibration pressures of >10–13 kbar, consistent with slab–mantle depths in the forearc (Coleman, 1961; Tsujimori et al., 2007). Moreover, isotope analyses of jadeite veins in the same metabasalts reveal heavy δ^7Li values and elevated concentrations of fluid mobile elements (FME) such as Li, Cs, Rb, and Ba, indicative of a slab-derived fluid source (Takahashi et al., 2018). Given that the exhumation of these high-density rocks may be explained by entrainment within rising buoyant serpentinite, and that these metabasalts retain a geochemical signature consistent with a slab source, it may be inferred that New Idria serpentinite rose from similar depths within the forearc mantle wedge.

The above geochemical, petrological, and structural evidence is complemented by thermodynamic, geophysical, and geodynamic arguments that theoretically support the existence of serpentinite diapirs in the forearc mantle wedge. Experimental and thermodynamic studies of ultramafic systems at pressures and temperatures constrained by thermal modeling of subduction zones suggest that serpentine-bearing assemblages are stable throughout the forearc mantle wedge (Spear, 1993; Syracuse et al., 2010; Ulmer and Trommsdorff, 1995). Seismic studies have detected pervasive low-velocity regions in the forearc mantle consistent with low-density serpentinization regimes (Hyndman and Peacock, 2003). The positive buoyancy required for the diapiric rise of serpentinite bodies is enabled by the increase of molar volume attending serpentinization (O'Hanley, 1996), which reduces serpentinite density relative to surrounding anhydrous lithologies. Serpentinites have been interpreted to rise buoyantly at a variety of tectonic settings, e.g., forearc seamounts (Murata et al., 2009), ophiolites (Schuiling, 2011), mid-ocean ridge systems (Bonatti, 1976), and in rift zones at the slab bend of downgoing oceanic lithosphere (Polonia et al., 2017).

Although the above evidence and theoretical arguments are consistent with a forearc mantle diapir model, the deep source hypothesis at New Idria has not been thoroughly tested by direct whole-rock elemental analyses of the serpentinites themselves. Such analyses are important because the results can be used to constrain the tectonic origins of serpentinites (Deschamps et al., 2013; Peters et al., 2017). Published geochemical data for New Idria serpentinites do not exist beyond 14 boron analyses of three proximate specimens in Yamada et al. (2019) and five whole-rock major element analyses by Van Baalen (1995). Low-B concentrations and isotopically light δ^{11}B in New Idria serpentinites are consistent with deep, ~2 GPa, slab-derived fluids (Yamada et al., 2019); however, the measured range overlaps significantly with serpentinites from ophiolites that have abyssal and/or supra-subduction origins that never experienced subduction (Martin et al., 2016). Similarly, elevated Cr# values in New Idria spinel grains are consistent with a mantle wedge setting, but also partially overlap an abyssal signature (Yamada et al., 2019). Altogether, these isotopic analyses combined with the association with blueschist and eclogite blocks provide evidence to support a mantle wedge origin hypothesis but are limited by ambiguity with other origins and by a small sample size.

Alternative hypotheses suggest the New Idria serpentinite protolith has an abyssal origin that was exhumed and serpentinized more recently. Coleman (1996) proposed that New Idria represents subducted abyssal Farallon slab that was wedged into the continental crust via sub-parallel thrusting and folding during the development of the San Andreas Fault system in the Miocene. Van Baalen (2004) describes the New Idria serpentinite as a fragment of supra-subduction zone mantle from the Coast Range Ophiolite emplaced prior to diapirism. Similarly, Vermeesch et al. (2006) suggested that the New Idria body was serpentinized around ~14 Ma following fluid infiltration associated with post-subduction tectonic activity along the San Andreas fault. Although not at New Idria, seismic evidence for a serpentinite diapir rising from the subducted slab through the accretionary prism of the Calabrian arc suggests an alternative emplacement mechanism that may apply (Polonia et al., 2017). All four of these scenarios imply that serpentinization could have occurred in an abyssal environment or other relatively shallow crustal setting since the initiation of the San Andreas Fault system. Such sources should be geochemically distinguishable from a mantle wedge environment using whole-rock elemental analyses.

Recent studies on global trends in serpentinite geochemistry reveal a diverse array of discriminating parameters that may be used to distinguish between serpentinites hydrated in the mantle wedge versus those formed in other tectonic settings (Deschamps et al., 2013; Kodolányi et al., 2012; Peters et al., 2017). These parameters may be divided into two components: constraints on the composition of the peridotitic protolith and constraints on the source of serpentinizing fluids. A mantle wedge protolith for forearc serpentinites may be distinguished by the putative concept that peridotites in arc melting regimes experience a greater degree of melt depletion relative to abyssal protoliths and that these depleted signatures are preserved by fluid-immobile elements that are largely unaffected by serpentinization. This results in a variety of distinct chemical signatures for serpentinites that reflect depleted source rock, e.g., higher MgO/SiO_2 and lower Al_2O_3/SiO_2, low Ti, and Cr-rich chromites (Deschamps et al., 2013). A slab-derived fluid signature in mantle wedge serpentinites is resolvable from other sources because slab fluids tend to be enriched in FMEs released from subducted sediments (Deschamps et al., 2013). If these fluids enter the forearc mantle wedge within the stability range of serpentine, then FME-rich serpentinites will form (Deschamps et al., 2010; Deschamps et al., 2011; Kodolányi et al., 2012; Peters et al., 2017; Scambelluri et al., 2004).

This broad array of geochemically discriminating whole-rock analyses has not yet been performed for New Idria despite lingering uncertainty regarding the source of the serpentinite body. To address this need, we present a suite of major, minor, and trace elemental whole-rock analyses of ten serpentinite samples distributed throughout the New Idria massif with the goal of constraining its tectonic origin. The results permit a multi-pronged test of the deep mantle wedge origin hypotheses favored by previous geochemical and petrologic studies (Takahashi et al., 2018; Tsujimori et al., 2007; Yamada et al., 2019). If supported, this would strengthen the interpretation that New Idria is a terrestrially accessible analog (Tsujimori et al., 2007) to the well-studied submarine serpentinite mud volcanoes along the Mariana forearc (Albers et al., 2020; Fryer et al., 1999; Murata et al., 2009; Savov et al., 2005). In addition to placing constraints on the geologic history of New Idria, this contribution may enhance our understanding of element cycling in continental forearc settings and of the broader Cenozoic tectonic and geologic history of the western margin of North America.

2. Geologic setting and sampling locations

The New Idria serpentinite body is located in the Diablo Range of central California, trending along N70°W, oblique to the nearby San Andreas fault. It is an oblong massif approximately 5–10 km wide and 20–25 km long, of comparable area to Mariana forearc submarine mud volcanoes (Savov et al., 2005) and physiographically distinct from the surrounding landforms (Fig. 1). New Idria lies in the fold of the Coalinga Anticline, flanked by the Mesozoic Franciscan Complex and Cretaceous marine siliceous sediments of the Panoche formation (Coleman, 1961). These relationships are shown in a simplified geologic map (Fig. 2), which also features selected strike and dip measurements that illustrate a dome structure in the surrounding layers. Some layers along the contact between New Idria and the Franciscan Complex are locally overturned, consistent with upward movement of a piercement structure (Coleman, 1961). Smaller outcrops of serpentinites on the western margin of the map do not have a direct structural relationship to New Idria.

The surface expression of New Idria is >99% serpentinite, mostly presenting as flaky, unconsolidated regolith exposed on barren, rounded, steep slopes (Fig. 3). In addition to occasional exposures of competent serpentinite bedrock, New Idria hosts a lithologically diverse array of minor blocks and outcrops from <1 m to 1500 m in length including jadeitite, blueschist, eclogite, rodingite, listvenite, unaltered peridotites, metagraywacke, and greenstone (Coleman, 1961; Tsujimori et al., 2007; Van Baalen, 1995). The jadeitites and high-grade metabasaltic tectonic blocks are found only in an isolated outcrop at Location A (Table 1, Fig. 2). A late, small syenite intrusion occurs in the southern part of the New Idria serpentinite body and is dated to 12 Ma (Tsujimori et al., 2007). Only massive, coherent serpentinites were collected for this study; other lithological blocks were avoided. The collection sites reflect a variety of locality types including knobby ridge tops, talus slopes, stream deposits, and an asbestos quarry (Fig. 2, Table 1). In order to assess trends across the New Idria massif, the sites were selected to expand the geographic range beyond the sampling area of Yamada et al.

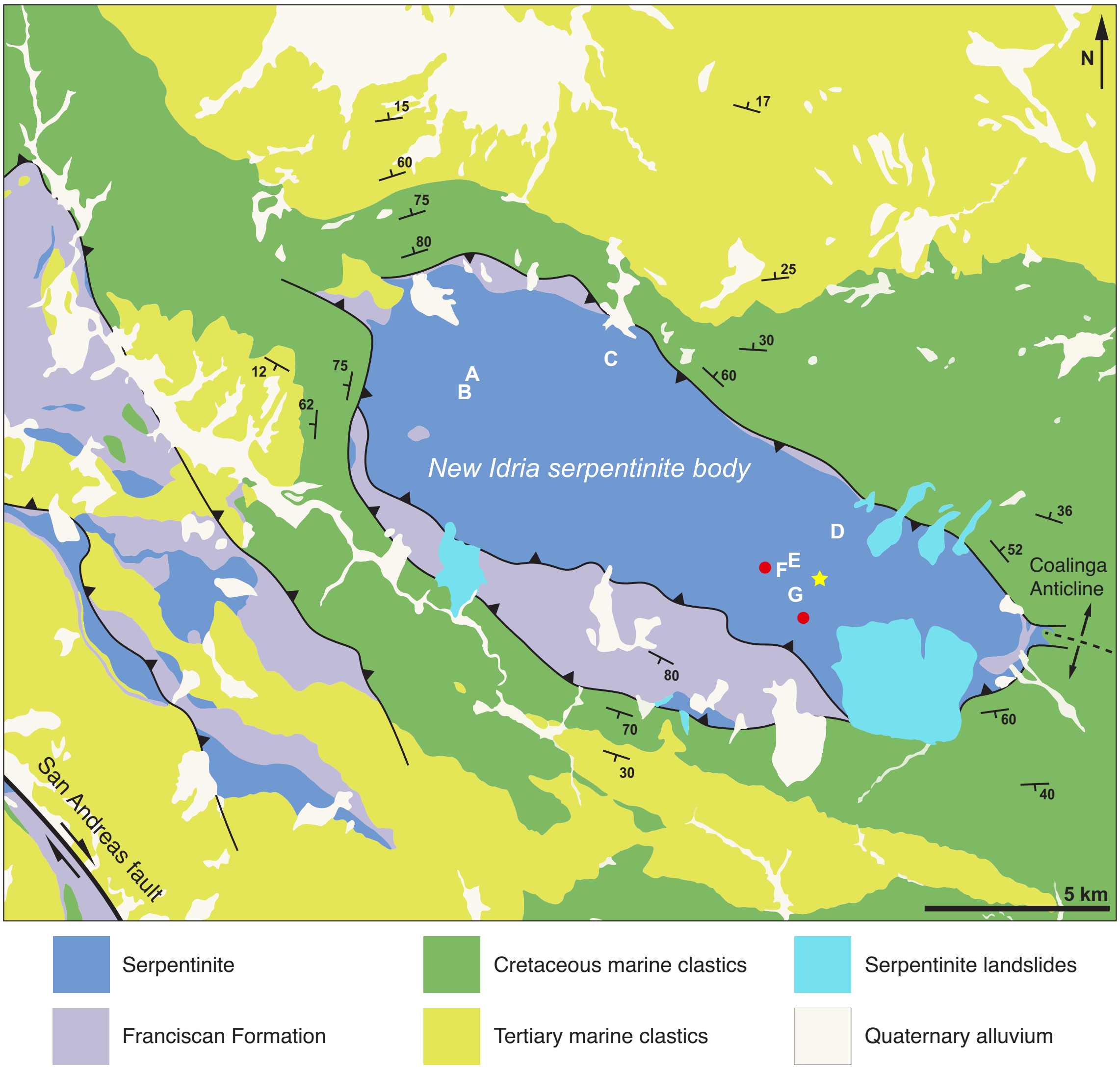

Fig. 2. Simplified geological map of the New Idria serpentinite body, San Benito County, California, adapted from the following 1:24,000 USGS quadrangle maps: Ciervo Mountain, Hepsedam Peak, Hernandez Reservoir, Idria, San Benito Mountain, and Santa Rita Peak. Bold white letters (A–G) are sampling locations, corresponding to specimens listed in Table 1. Location A also denotes the site of exposed metabasaltic tectonic blocks described by Tsujimori et al. (2007). Red dots: syenite intrusions. Yellow star: the "Gem Mine", a benitoite quarry.

Fig. 3. Representative field photograph depicting the predominant physiography and barren regolith of the New Idria serpentinite body. Location: 36.378° N, 120.728° W.

(2019), which roughly corresponds to locations A and B.

3. Analytical methods

All samples were trimmed with a rock saw and well-sonicated to remove weathering rinds and other contaminants prior to analysis. Major, minor, and accessory minerals were identified by a combination of x-ray diffraction (XRD), scanning electron microscope (SEM) with energy dispersive x-ray spectroscopy (EDS), and reflected and polarized light microscopy at California State University, San Bernardino. Chromium number (Cr#) values for chromite were determined using EDS, where $Cr\# = \%Cr \div (\%Cr + \%Al)$ in atomic percent. An EDS calibration curve was constructed by analyzing chromites from a komatiite whose compositions were previously quantified by electron microprobe (Lazar et al., 2012).

Whole-rock elemental concentrations were measured by x-ray fluorescence (XRF) and inductively coupled plasma mass spectrometry (ICP-MS) at the Washington State University (WSU) GeoAnalytical Lab (Johnson et al., 1999; Knaack et al., 1994). Handpicked sample chips were ground in a tungsten carbide swing mill for 2 min to an average grain size of ~10 μm. A subsample of the powder was mixed at a 2:1 ratio with lithium tetraborate flux ($Li_2B_4O_7$) in a plastic vessel for 10 min. The powder was placed into a carbon crucible and fused into a glass bead in a preheated muffle furnace at 1000 °C. Fused beads were reground for homogenization and to split a portion of the powder for ICP-MS analysis. The remaining material was re-fused, polished, and loaded into a ThermoARL Advant'XP+ sequential XRF spectrometer. ICP-MS powders were processed by open-vial dissolution involving sequential digestions and evaporations in concentrated nitric (HNO_3), perchloric ($HClO_4$) and hydrofluoric (HF) acids. The resulting solutions were diluted by a factor of ~3400 for analysis on an Agilent 7700x quadrupole ICP-MS.

To demonstrate the stability and accuracy of the XRF, Table S5 provides five analyses of the USGS standard basalt BCR-2 from the days surrounding the analysis dates of the present study. All analyses reproduce within ≤1% over the course of the time series.

Accuracy during ICP-MS analysis was assessed by comparing internal analyses of BCR-2 to the values of Wilson (1997) for all elements and oxides except Nb and Ta which were compared to the analyses of Nagaishi and Ishikawa (2009) (Fig. S1 and Table S1 in Supplementary Material). The relative difference between BCR-2 in the analytical run and the published reference values was <5% for all elements except Cr (11%), Ni (6%), Cu (11%), Ga (10%), and Cs (11%). Additionally, as a measure of the overall analytical reproducibility of the facility, long term standard monitoring provided by WSU (Table S2) shows the relative standard deviation of 50 analyses over five years of the USGS igneous reference standard andesite AGV-1 and the relative percent difference (%RPD) between repeat pairs averaged for 500 unknown samples over five years (Table S2). Both of these metrics report long-term precisions of < 2.5% for all elements, with the exception of Sc (%RPD = 4.06%).

Instrumental precision during the analytical run was estimated by replicate analyses of two New Idria specimens, AM1 and COL1 (Table S3; Fig. S1). AM1 had a ≤ 4% difference between replicates for all elements except Sm, Eu, Tb, Dy, Ho, Tm, and Ta, which showed percent differences that ranged from 4.1–13.7%. COL1 replicates show larger percent differences, from <1% to >50% for Sm, Ho, and Tm. The majority of elements have percent differences that fall between 2 and 23%.

Detection limits for ICP-MS are provided in Table S4, computed using calibration curves anchored to blank analyses. XRF detection limits for TiO_2 were reported to be 0.017 wt% by the WSU laboratory based on drift during the analytical runs. However, repeat TiO_2 analyses of COL1 were 0.006 and 0.005 wt%, a difference of 0.001 wt% (18%). This may suggest that the 0.017 wt% detection limit is overestimated;

Table 1
Sample locations and descriptions.

Location in Fig. 2	Location	Brief outcrop description	Specimen	Brief hand sample description
A	36.3837°N 120.7219°W	Boulder in stream	COL1	Green with weakly aligned magnetite-rich veins [NOTE: sample is near the exposure of the high-grade metabasaltic tectonic blocks described in Tsujimori et al., 2007]
B	36.3824°N 120.7225°W	Boulders from talus slope	HSP18B	Shiny dark green-blue, hard, fine-grained mesh texture, slickensides, minor light-green <1 mm serpentine veins
C	36.3901°N 120.6750°W	Resistant knob on barren hilltop	N1R1C	Dark green, hard, fine-grained mesh texture
D	36.3468°N 120.6020°W	Resistant ridge on Santa Rita Peak	SP1B	Black to very dark green, hard, andradite veins
E	36.3396°N 120.6159°W	Boulders exposed at the KCAC asbestos mine	SAM	Fine-grained translucent light green serpentine with dark magnetite-rich spots and light calcitic clusters minor light green <1 mm serpentine veins
			AM1	Mottled green with slickensides, complex structure, pervasively veined with light-green serpentine
F	36.3385°N 120.6192°W	Cobbles and boulders along a wash	MM21	Dark green, hard, bastitic, coarse relict peridotitic texture, mesh texture
			SM41-1	Black to very dark green, hard, bastitic, coarse relict peridotitic texture, mesh texture
			SM52	Dark green, hard, fine-grained mesh texture
G	36.3325°N 120.6150°W	Resistant outcrop on a hilltop	RH8	Light green, weakly subparallel magnetite veins

nevertheless, we conservatively adopted this value, as shown in in Fig. 6.

4. Results

Petrographic analyses showed that all rocks were fully serpentinized except MM21 and SM41-1, which contained relict olivine and pyroxene (Table 2). Antigorite was detected in 3 of 10 specimens: COL1, SM52, and SP1B. Brucite was detected in 7 of 10 specimens. Transition metal accessory minerals were present in all specimens, including isolated magnetite grains and veins, magnetite-rimmed chromite, and a variety of Ni- and Co-bearing phases including awaruite (Ni_3Fe), heazlewoodite (Ni_3S_2), pentlandite ($(Fe,Ni,Co)_9S_8$), millerite (NiS), and jaipurite (CoS) (Fig. 4). Minor silicate minerals include andradite and chlorite in multiple specimens and an unspecified Na–Ca amphibole in one specimen (MM21, Fig. 4f). Chromites are present in all rocks, with Cr# values ranging from 0.29 to 0.83 (Table 2). Redistribution of Cr was observed in several samples, expressed as variable Cr# in chromite, reactive intergrowths of Cr-bearing andradite and chromite (Fig. 4b), and Cr-bearing serpentine and chlorite. One grain of barite was observed in SP1B (Fig. 4d). Minor calcite was observed in two specimens, AM1 and SAM, in both cases with a highly reactive texture (Fig. 4e).

Whole-rock major elemental concentrations (Table 3) have typical serpentinite compositions: high in MgO (~37–44 wt%, %RSD = 5) and low in SiO_2 (~30–41%, %RSD = 9). Titanium is a useful diagnostic species for serpentinite discrimination diagrams; however, all but one of the reported TiO_2 concentrations are below detection, placing a conservative upper limit in those specimens of 0.017%. Na_2O and K_2O, which in principle could correlate to trace alkali FMEs, are both below detection in all but two samples: MM21 and SM41-1.

Whole-rock trace element concentrations (Table 3) range from 10^3 ppm to below detection. Transition metals (Sc, V, Cr, Ni, Cu, Zn) including high field strength elements (HFSE: Zr, Nb, Hf, Ta, Th) have, on average, the lowest variability, where %RSD for these elements ranges from 14 to 67%. Zirconium and hafnium have comparatively high average concentrations: respectively, 3.1 and 0.06 ppm. Low relative concentrations of Nb and Ta result in elevated $HFSE^{+4}/HFSE^{+5}$ ratios (Table 4), with Zr/Nb as high as ~158. Fluid mobile elements (Cs, Rb, Sr, Ba, Pb) are quite variable, with %RSD = 103–248. As will be illustrated below, some FME concentrations rank among the highest ever measured in serpentinites, with Cs as high as 6.4 ppm and Ba as high as ~67 ppm. Uranium, which can be a FME, has a %RSD of 69, more consistent with the variability of the transition metals than the FMEs. Concentrations of U are on the order of 0.01 ppm. All trace element concentrations are generally above detection limits, except for most Eu analyses and a few heavy REE analyses (Table 3). Also, four of ten Ta analyses are at the detection limit, with the remainder very near the limit.

5. Discussion

The subsequent sections focus on comparing the New Idria serpentinite results to global datasets of whole-rock serpentinite compositions grouped by two tectonic signatures: abyssal systems and the mantle wedge (Deschamps et al., 2013; Peters et al., 2017). The term *abyssal* refers to specimens that are serpentinized on or beneath the ocean floor. The abyssal datasets considered in this study include whole-rock serpentinite samples mostly from slow to ultraslow spreading ridges where serpentinites are more commonly sampled. The term *mantle wedge* refers to the mantle region in a subduction zone below the crust of the overlying plate and above the slab-mantle interface where serpentinization is initiated by fluids emerging from the subducted slab. The mantle wedge serpentinite datasets include modern active forearc serpentinites from the Izu–Bonin–Mariana arc system, Guatemala, and South Sandwich Islands, and also tectonically emplaced bodies from New Caledonia,

Table 2
Petrographic and mineralogical analyses of New Idria serpentinites.

Specimen	Major and minor minerals	Accessory minerals	Chromite Cr# ± 1sd	Notes
AM1	Lizardite, brucite Magnetite, chromite	Heazlewoodite Pentlandite (rare) Calcite	0.71 ± 0.03	100% serpentinized. Isolated calcite (avg. 50–200 μm) with secondary reactive internal sieve-like texture containing recrystallized serpentine (Fig. 4e).
COL1	Antigorite, lizardite Brucite, magnetite Andradite, chromite	Awaruite Heazlewoodite Pentlandite	0.70 ± 0.02	100% serpentinized. Some chromites show irregular reactive intergrowth textures with Cr-bearing andradite (Fig. 4b).
HSP18B	Lizardite, andradite Magnetite, chromite	Awaruite, pentlandite Heazlewoodite Jaipurite (CoS, rare)	0.66 ± 0.05	100% serpentinized. Significant Co and Cu substitution in accessory minerals. Chromite contains minor Mn. Andradite contains minor Cr. Serpentine contains minor Cr and Al.
MM21	Lizardite, brucite Olivine, enstatite Magnetite, chromite Ca-Na amphibole	Awaruite, unidentified sulfide (rare)	0.49 ± 0.03	20–30% serpentinized. Reflective Fe-rich reaction rims surround enstatite. Ca–Na-Mg-silicate in veins and along enstatite margins (Fig. 4f). Serpentine contains 1–2% Cr
N1R1C	Lizardite, brucite magnetite, chromite	Awaruite, pentlandite Heazlewoodite Co-pentlandite	0.74 ± 0.03	100% serpentinized. Chromite image in Fig. 4c.
RH8	lizardite, magnetite Chromite	awaruite, pentlandite Native Copper (rare) Heazlewoodite (rare)	variable	100% serpentinized. Reactive textures around magnetite veins and crystals, with reflective Fe-bearing gradients penetrating surrounding serpentine. Chromites have variable Cr# (0.38–0.78) with several clustered around a maximum Cr# of 0.72; some are partially to completely replaced by Cr-bearing serpentine (Fig. 4a).
SAM	Lizardite, brucite Magnetite, chlorite Chromite, calcite Cr-andradite	Heazlewoodite	0.57 ± 0.02	100% serpentinized. Abundant dendritic, sieved calcite with reaction textures, intergrown with brucite and magnetite (Fig. 4e). Calcite growth in serpentine and along veins. Chromites have Cr-andradite rims overgrown by magnetite.
SM41–1	Lizardite, brucite Olivine, enstatite Diopside, magnetite Chromite	Awaruite Heazlewoodite	0.29 ± 0.03	50–70% serpentinized. Enstatite with minor Cr and Al; diopside with minor Al.
SM52	Lizardite, antigorite Brucite, magnetite Chromite	Awaruite	0.65 ± 0.03	100% serpentinized.
SP1B	Antigorite, magnetite chromite, chlorite Cr-andradite	Barite, millerite (rare) Heazlewoodite (rare) Ni-arsenide (rare)	0.83 ± 0.03	100% serpentinized harzburgite. Chromites contain minor Mn. Reactive intergrowths of magnetite, chromite, Cr-bearing chlorite, Cr-bearing serpentine. Barite in Fig. 4d.

India, and Cuba.

Some authors refer to the mantle wedge setting as the forearc mantle wedge or simply the forearc. However, this introduces terminological imprecision when discussing the petrogenetic origin of a serpentinite because “forearc” is a geographic term for the region between the trench and the volcanic arc, which technically can contain serpentinites of other tectonic origins, e.g., abyssal serpentinites entrained in the accretionary prism. Therefore, we use *forearc* as a geographic term and use *mantle wedge* when referring to the origin of the protolith and location of serpentinization.

5.1. Whole-rock analyses: major and minor elements

A MgO/SiO_2 versus Al_2O_3/SiO_2 plot is commonly used to distinguish between the tectonic origin of serpentinites (Fig. 5) (Cooperdock et al., 2018; Deschamps et al., 2013; Kodolányi et al., 2012; Niu, 2004). The global compositional ranges of mantle wedge serpentinites and abyssal serpentinites occupy different regions of the diagram, with >95% of mantle wedge rocks occupying a range of high MgO/SiO_2 (~0.8–1.5) and low Al_2O_3/SiO_2 ($\sim 10^{-4}$ to 0.04). Abyssal rocks occupy a comparatively larger range of compositions that partly overlap the mantle wedge values but also trend toward lower MgO/SiO_2 (0.5–1.2) and higher Al_2O_3/SiO_2 ($\sim 10^{-3}$ to 0.09). A canonical explanation for this difference is that mantle wedge serpentinites retain, on average, melt-depleted, refractory peridotitic compositions of high MgO/SiO_2 and low Al_2O_3/SiO_2 compared to rocks from abyssal settings, likely due to higher degrees of H_2O-fluxed partial melting in arc systems. This interpretation implies that major element compositions of peridotites are largely unaffected by serpentinization or post-metamorphic processes; however, the details underpinning this assumption are complicated by reports of post-serpentinization MgO loss and/or SiO_2 gain in abyssal serpentinites (Malvoisin, 2015; Paulick et al., 2006; Snow and Dick, 1995) or silica metasomatism in the mantle wedge (Kawahara et al., 2016). Such processes create scatter around the narrow terrestrial array of purely magmatically fractionated compositions (dashed line, Fig. 5).

Nevertheless, the empirical signatures in the global datasets permit first-order distinctions between the compositional ranges of mantle wedge and abyssal serpentinites. The distribution of values within the New Idria dataset more closely corresponds, in aggregate, to the mantle wedge range than to the abyssal range (Fig. 5). Although several New Idria values overlap both the mantle wedge and abyssal ranges, there is no New Idria composition that can be unambiguously assigned to an abyssal signature. Moreover, one specimen (SAM, $MgO/SiO_2 > 1.4$) has an extremely depleted composition that is well outside the distribution of abyssal values, and two specimens (N1R1C & COL1, $MgO/SiO_2 \sim 1.2$) have compositions that only overlap the most depleted endmember of the abyssal signature.

The presence or absence of brucite is a metamorphic expression of bulk compositional effects influenced by the degree of melt depletion of the protolith. To a first order, brucite-bearing serpentinites form by metamorphism of highly melt-depleted, high MgO/SiO_2 protoliths with excess olivine over enstatite via the following model reaction:

$$2Mg_2SiO_{4\ (olivine)} + 3H_2O \Leftrightarrow Mg_3Si_2O_5(OH)_{4\ (serpentine)} + Mg(OH)_{2\ (brucite)} \tag{1}$$

By contrast, less-depleted protoliths marked by lower MgO/SiO_2 can contain enough enstatite to prevent brucite formation via the following model reaction:

$$Mg_2SiO_{4\ (olivine)} + MgSiO_{3\ (enstatite)} + 2H_2O \Leftrightarrow Mg_3Si_2O_5(OH)_{4\ (serpentine)} \tag{2}$$

In summary, brucite is favored during serpentinization of highly depleted protoliths with high MgO/SiO_2, e.g. dunites. This relationship is delineated in Fig. 5, where brucite-bearing specimens (closed circles) have high MgO/SiO_2 (> 1) values that are distinct from the cluster of less depleted values corresponding to the brucite-free specimens (open circles). Because serpentinization of highly depleted mantle wedge protoliths should favor brucite stabilization, the lack of brucite in some New Idria samples may suggest brucite destabilization by the addition of aqueous silica in metasomatic fluids (Kawahara et al., 2016) via reactions such as:

$$3\ Mg(OH)_{2\ (brucite)} + 2SiO_{2(aq)} \Leftrightarrow Mg_3Si_2O_5(OH)_{4\ (serpentine)} + H_2O \tag{3}$$

Elevated SiO_2 would drive MgO/SiO_2 to lower values and would help explain why the brucite-free rocks fall below the terrestrial array, implying the possibility that metasomatic silica may have erased an earlier highly depleted brucite-bearing serpentinite assemblage. Alternatively, these samples may have always been brucite-free. Regardless of the reason for the absence of brucite, the brucite-free specimens remain within the bounds of the global mantle wedge signature, albeit near the periphery.

The relationship between TiO_2 and MgO may also be used to differentiate between mantle wedge and abyssal signatures, as shown by the discrimination diagram in Fig. 6. In general, partial melting imparts an inverse relationship between MgO and TiO_2 in the residual mantle, with depleted peridotites characterized by high MgO and low TiO_2. Consistent with the above arguments in the MgO-SiO_2-Al_2O_3 system, mantle wedge protoliths are considered to be more depleted than abyssal protoliths (Deschamps et al., 2013; Niu, 2004), as expressed by the distribution of global mantle wedge serpentinite values toward higher MgO (~39–53%, mean: 46%) and lower TiO_2 (~0.001–0.1%, mean: 0.016%) compared to abyssal values, where MgO = ~30–49% (mean: 43%) and TiO_2 = ~0.005–0.07% (mean: 0.025%). Within this framework, the New Idria TiO_2–MgO data favor a mantle wedge signature. Values of MgO for three of the New Idria specimens exceed the highest values of the global abyssal dataset, and all MgO values exceed the average global abyssal value. For all but one specimen, the nominal TiO_2 values are below the 0.017% reported analytical detection limit, which constrains the New Idria values to coincide with the most extremely depleted mantle wedge values.

5.2. Whole-rock analyses: trace elements

5.2.1. Fluid mobile elements

Fluid mobile element (FME) signatures are useful for distinguishing between serpentinites that are hydrated by seawater in an abyssal setting from those hydrated by slab-derived fluids, e.g., in the mantle wedge (Deschamps et al., 2010, 2011, 2013; Kodolányi et al., 2012; Peters et al., 2017; Savov et al., 2005). The New Idria dataset shows distinct enrichments in Cs, Ba, and Rb characteristic of a mantle wedge protolith serpentinized by fluids emanating from the subducting slab, as supported by a series of discrimination diagrams that distinguish between tectonic origin. The plots in Fig. 7 compare FME behavior to a representative fluid-immobile element, Yb. Of these FME–Yb relationships, the Cs systematics (Fig. 7a) are the most clearly resolved between the global abyssal and mantle wedge datasets with little overlap between the two sources. The New Idria specimens are well-matched to the mantle wedge signature, with 8 of 10 serpentinites exhibiting Cs concentrations greater than ~95% of the global abyssal concentrations and Cs/Yb ratios greater than ~85% of the global abyssal ratios. Two samples contain particularly high Cs concentrations: N1R1C and SM41-1, with respective values of 6.44 ppm and 2.85 ppm. These Cs enrichments exceed all other reported values for mantle wedge serpentinites in the global dataset ($n = 169$ analyses) (Deschamps et al., 2013). Moreover, these two New Idria values rank in the five highest measurements for all global serpentinites regardless of tectonic setting ($n = 350$).

Global Ba/Yb vs. Ba systematics do not delineate tectonic setting as clearly as the Cs signatures, as expressed by a larger proportion of overlap between mantle wedge and abyssal signatures (Fig. 7b). Nevertheless, a mantle wedge signature may be partly distinguished

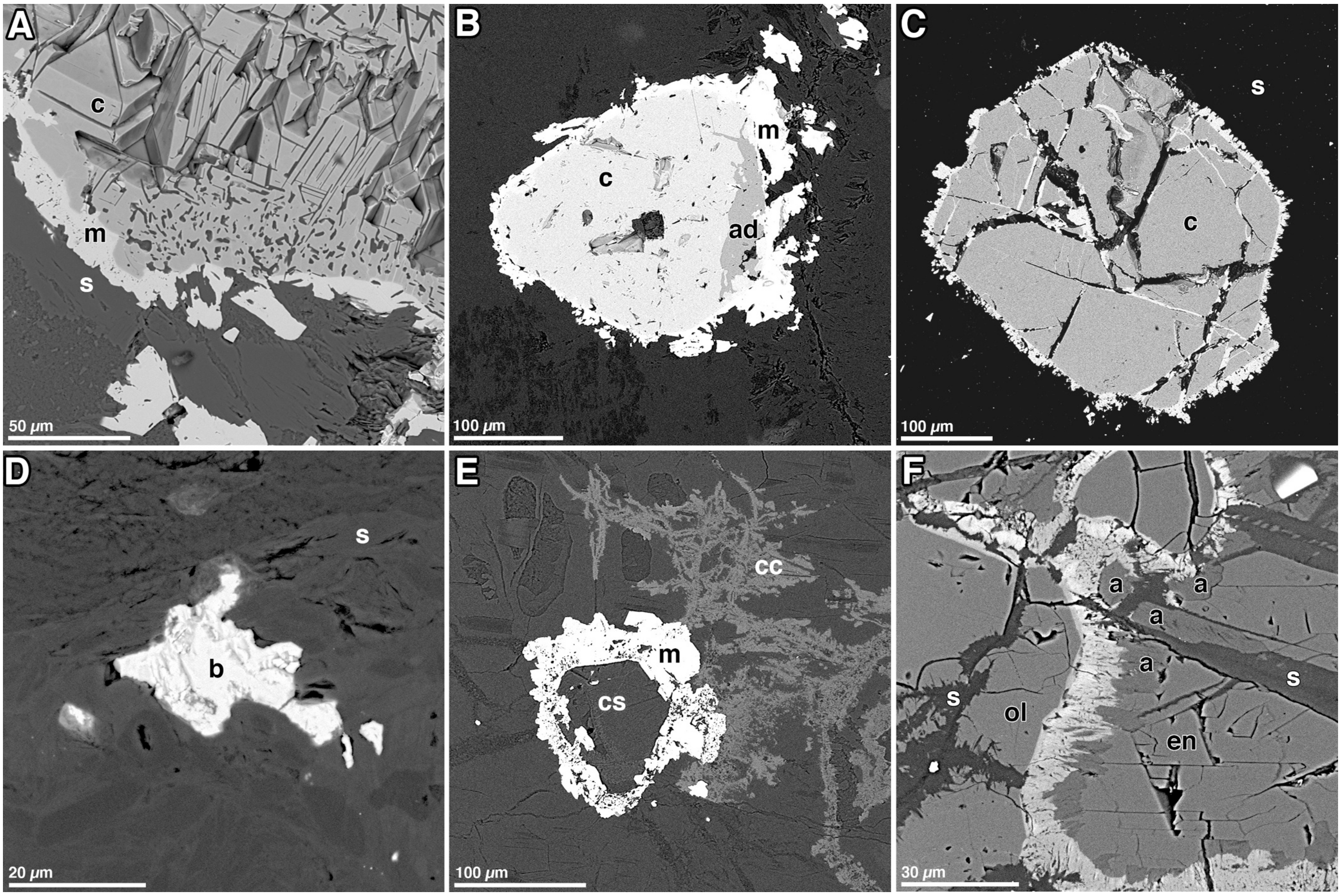

Fig. 4. Backscattered SEM images from selected serpentinite specimens. *A*. Reaction textures between chromite, magnetite, and serpentine in RH8. *B*. Replacement of chromite with Cr-rich andradite and magnetite rim in COL1. *C*. Chromite with reflective magnetite overgrowth from N1R1C. *D*. Barite crystal surrounded by serpentine in SP1B. *E*. Secondary calcite growth in serpentine with Cr-bearing serpentine pseudomorph after chromite and magnetite rim in SAM. *F*. Enstatite and olivine with metamorphic overgrowth of serpentine, Fe-rich reaction rim (white/light gray), and a NaCa amphibole] in MM21. Abbreviations: a = amphibole, ad = andradite, b = barite, c = chromite, cc = calcite, cs = Cr-bearing serpentinite, en = enstatite, m = magnetite, ol = olivine, s = serpentine,

from abyssal values by a more restricted overall range in values: e.g., most mantle wedge values exist over a log Ba/Yb range of 1–3 but abyssal values are evenly distributed over a log Ba/Yb range of 0–3. All of the New Idria data fall within the more limited mantle wedge range and no data have an exclusively abyssal signature. Also, a linear regression of the mantle wedge dataset (brown line) has Ba/Yb values that are ~0.5–0.8 log units greater than the abyssal trend (blue line) (Fig. 7b). Linear regression of the New Idria data (black line) results in a trend that is within the standard error of regression of the mantle wedge data and statistically distinguishable from the regressed trend of the abyssal data (Fig. 7b & S2).

As with Cs, enriched Ba appears to be an important component of the New Idria geochemical signature (Figs. 7–10). Six New Idria specimens contain Ba concentrations in the top 25 of the global mantle wedge serpentinite dataset ($n = 307$). In specimen SP1B, Ba is sufficiently concentrated that the mineral barite is saturated (Fig. 4d). Rb behavior is more variable and less enriched than Cs or Ba, although three samples have Rb concentrations in the top 20% of global mantle wedge values ($n = 233$). A plot of Rb/Yb vs. Rb shows that these three specimens (log Rb/Yb > 1.5) are only consistent with a mantle wedge origin (Fig. 7c). Most of the remaining specimens have Rb values that are consistent with a mantle wedge origin, although not definitive owing to overlap with the abyssal signature. Uranium concentrations do not strongly correlate to either signature, instead occupying a range of values intermediate to the mantle wedge and abyssal settings (Fig. 7d). The LILEs Sr and Pb are enriched, although these elements are also characteristically high in abyssal settings and, therefore, are not definitive of slab fluids and a mantle wedge source (Fig. 8).

Values of the ratio Rb/Cs may place constraints on the depth of serpentinization within the wedge and the source of the serpentinizing fluid, as suggested by a recent field study of serpentinite mud volcanoes along the Mariana forearc (Albers et al., 2020). In this study, serpentinites formed at 13 km depth contained Rb/Cs $\gg 10$ and were interpreted to be hydrated by fluids sourced from sedimentary pore waters expelled at shallow depths. Specimens formed at 14–18 km contained Rb/Cs < 5 and were interpreted to be serpentinized by slab-derived fluids sourced from dehydrated sediments and oceanic crust at greater depths. At New Idria, Rb/Cs values range from 0.4 to 5.8 with an average value of 1.9 (Table 4), which is consistent with a sediment- and/or crust-derived fluid source as inferred for the deeper (>13 km) Marianas serpentinites.

Although serpentinization by an FME-rich fluid can explain the observed enrichments in Cs, Ba, and Rb, these fluid mobile elements are also magmatically incompatible during partial melting of the mantle. Therefore, an alternative explanation for the New Idria signatures could be infiltration of the protolith by Cs-, Ba-, and Rb-rich melts. This potential for magmatic FME signatures was explored using plots of Cs and Ba versus Yb, a fluid immobile, conservative element that only fractionates significantly during melting (Fig. 9). If the New Idria specimens contain Cs and Ba concentrations that are genetically related to melt–rock interactions, then these values should correlate to Yb. However, the scattered data in Fig. 9 show no such correlation, suggesting

Table 3
Whole rock elemental concentrations in New Idria serpentinites. Major element concentrations measured via XRF.

	AM1	COL1	HSP18B	MM21	N1R1C	RH8	SAM	SM41-1	SM52	SP1B	Limit[b]	%RSD
Major elements (weight percent)												
SiO_2	36.22	34.82	40.96	39.90	34.36	39.06	29.82	38.79	37.87	40.61		9
TiO_2	*0.01*	*0.01*	*0.01*	*0.01*	*0.01*	0.05	*0.01*	*0.01*	*0.01*	*0.01*	0.02	106
Al_2O_3	0.32	0.09	0.55	0.43	0.02	0.71	0.37	0.72	0.17	1.34		83
FeO[a]	8.11	7.14	4.44	7.39	6.17	8.01	6.92	7.03	5.74	6.64		16
MnO	0.10	0.14	0.11	0.11	0.10	0.05	0.20	0.11	0.11	0.10		32
MgO	38.90	42.51	38.82	40.84	41.89	36.94	43.73	39.78	40.96	38.38		5
CaO	0.55	0.00	0.13	0.51	0.09	0.01	0.78	0.73	0.05	0.01		111
Na_2O	0.00	0.00	0.00	0.29	0.00	0.00	0.00	0.00	0.00	0.00		316
K_2O	0.00	0.00	0.00	0.02	0.00	0.00	0.00	0.01	0.00	0.00		184
P_2O_5	0.02	0.00	0.00	0.00	0.00	0.00	0.00	0.00	0.00	0.00		180
Sum	84.23	84.70	85.03	89.50	82.64	84.84	81.83	87.18	84.91	87.10		
LOI%	14.88	14.16	13.97	9.47	16.45	14.19	17.42	11.78	14.03	12.00		
Total	99.11	98.86	99.00	98.97	99.08	99.02	99.25	98.96	98.93	99.10		
Minor and trace elements (ppm)												
Sc	5.49	2.65	7.48	8.01	2.70	6.40	3.61	8.42	4.34	8.22	0.310	40
V*	23.9	13.6	31.0	36.0	9.3	24.7	23.0	37.0	20.3	38.0		38
Cr*	2530	2910	3410	3300	1970	3070	1810	2540	2790	2370		20
Ni*	2390	2570	2300	2150	2320	3050	3020	2180	2350	2090		14
Cu*	5.27	6.31	15.78	4.87	6.50	8.55	5.61	11.80	5.69	10.78		44
Zn*	47.1	35.0	31.4	42.4	30.1	22.9	42.1	37.2	41.2	37.9		19
Ga*	1.129	0.834	0.885	0.650	0.186	1.693	0.754	0.740	0.794	2.045		55
Rb	0.190	0.098	0.069	0.889	1.095	0.049	0.075	1.394	0.077	0.242	0.047	121
Sr	19.64	1.83	0.50	0.78	1.37	0.83	1.19	2.08	3.87	2.19	0.135	169
Y	0.190	0.094	0.114	0.068	0.060	0.869	0.068	0.142	0.069	0.235	0.014	129
Zr	4.81	3.21	4.21	3.08	3.09	3.06	2.46	2.16	2.48	2.59	0.211	27
Nb	0.079	0.032	0.027	0.029	0.022	0.027	0.019	0.045	0.029	0.020	0.004	54
Cs	0.086	0.017	0.183	0.302	6.442	0.015	0.044	2.854	0.049	0.248	0.013	204
Ba	66.93	4.30	4.80	1.01	40.60	2.71	53.59	30.59	5.61	20.55	0.155	103
La	0.279	0.12	0.073	0.077	0.078	0.074	0.051	0.085	0.075	0.097	0.010	65
Ce	0.600	0.262	0.151	0.182	0.167	0.194	0.112	0.181	0.149	0.167	0.010	65
Pr	0.055	0.026	0.018	0.018	0.015	0.019	0.009	0.020	0.015	0.013	0.005	62
Nd	0.206	0.096	0.043	0.066	0.059	0.105	0.030	0.092	0.053	0.048	0.022	64
Sm	0.056	0.048	0.025	0.016	0.006	0.058	0.013	0.025	0.011	0.023	0.006	68
Eu	*0.003*	*0.003*	*0.002*	b.d	*0.001*	0.021	b.d	b.d	b.d	*0.001*	0.010	–
Gd	0.037	0.017	0.012	0.007	0.011	0.078	0.010	0.016	0.010	0.031	0.006	94
Tb	0.007	0.003	0.002	0.002	0.004	0.017	*0.001*	0.003	0.002	0.005	0.002	101
Dy	0.039	0.025	0.020	0.012	0.008	0.138	0.014	0.018	0.010	0.042	0.003	120
Ho	0.007	0.005	0.004	0.002	*0.001*	0.028	0.002	0.004	*0.001*	0.012	0.002	127
Er	0.024	0.013	0.021	0.010	0.010	0.109	0.011	0.014	0.008	0.041	0.005	118
Tm	0.005	0.001	0.003	0.002	0.001	0.014	0.002	0.002	0.002	0.005	0.001	110
Yb	0.035	0.013	0.019	0.020	0.008	0.101	0.012	0.033	0.008	0.040	0.005	96
Lu	0.006	0.002	0.006	0.006	0.001	0.016	0.002	0.005	0.002	0.009	0.000	79
Hf	0.114	0.069	0.077	0.045	0.044	0.054	0.035	0.043	*0.031*	0.046	0.033	45
Ta	0.007	0.004	0.002	0.003	0.003	0.001	0.001	0.003	0.003	0.001	0.001	67
Pb	2.325	0.077	*0.032*	*0.018*	0.055	0.139	0.063	0.053	0.046	0.084	0.045	248
Th	0.154	0.063	0.046	0.049	0.041	0.041	0.033	0.037	0.031	0.052	0.005	66
U	0.050	0.017	0.013	0.014	0.014	0.013	0.010	0.011	0.013	0.016	0.004	69

Minor and trace elements measured via XRF(*) or ICP-MS.

[a] Total Fe. Analytical parameters, including detection limits, standard measurements, and reproducibility are provided in Supplemental Data.

[b] Limit = detection limit, for more detailed listing by mass see Table S3. Italicized values are below the reported detected limit. %RSD = relative standard deviation (100*stdev/mean).

Table 4
Selected whole-rock elemental and oxide ratios in New Idria serpentinite specimens, primitive mantle (PM, Sun and McDonough, 1989), depleted mantle (Salters and Stracke, 2004), and average N-MORB (Gale et al., 2013).

Ratio	AM1	COL-1	HSP18B	MM21	N1-R1C	RH8	SAM	SM-41-1	SM-52	SP1B	PM	DM	N-MORB
Al_2O_3/SiO_2	0.009	0.003	0.013	0.011	0.001	0.018	0.013	0.019	0.004	0.033	0.10	0.10	0.30
Ba/Yb	1918.89	343.21	246.52	51.92	4943.16	26.97	4530.78	924.00	701.86	512.97	14.18	2.99	5.98
Cs/Th	0.56	0.27	3.94	6.16	158.06	0.38	1.34	78.01	1.57	4.77	0.09	0.10	0.10
Cs/Yb	2.46	1.35	9.38	15.50	784.26	0.15	3.74	86.20	6.17	6.20	0.02	0.003	0.01
Hf/Nb	1.45	2.17	2.87	1.53	1.97	2.03	1.84	0.96	1.08	2.34	0.43	0.95	0.68
La/Yb	7.99	9.47	3.73	3.94	9.48	0.73	4.30	2.57	9.40	2.42	1.39	0.58	1.28
MgO/SiO_2	1.07	1.22	0.95	1.02	1.22	0.95	1.47	1.03	1.08	0.94	0.84	0.85	0.15
Rb/Cs	2.22	5.81	0.38	2.94	0.17	3.20	1.70	0.49	1.56	0.97	80.38	66.67	76.67
Ta/Yb	0.21	0.28	0.13	0.14	0.36	0.01	0.08	0.08	0.33	0.03	0.08	0.03	0.07
Th/Yb	4.43	5.04	2.38	2.52	4.96	0.40	2.80	1.10	3.92	1.30	0.17	0.03	0.08
U/Th	0.32	0.27	0.29	0.28	0.35	0.33	0.29	0.29	0.41	0.30	0.25	0.34	0.33
U/Yb	1.43	1.38	0.68	0.70	1.74	0.13	0.82	0.32	1.62	0.39	0.04	0.01	0.03
Zr/Nb	61.06	101.15	157.64	104.44	139.57	114.49	130.27	47.70	86.02	132.74	15.71	37.81	28.15

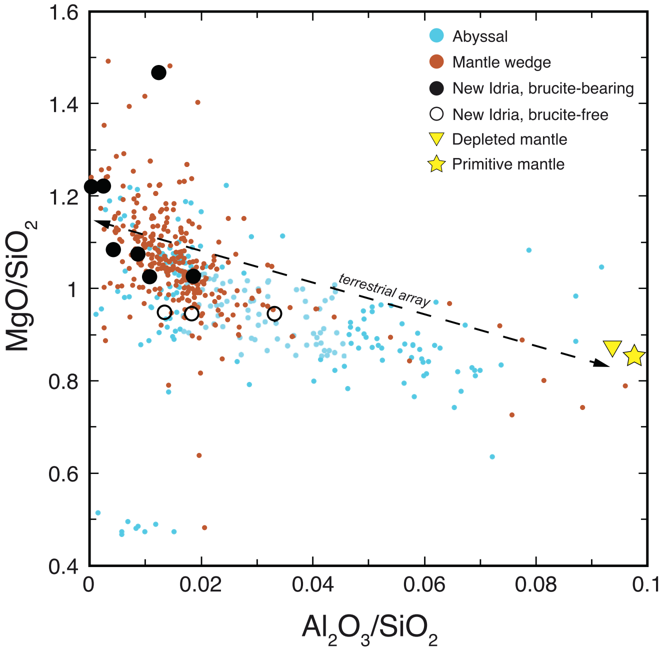

Fig. 5. MgO/SiO_2 versus Al_2O_3/SiO_2 (wt%) for New Idria and the global dataset of abyssal and mantle wedge serpentinites compiled in Deschamps et al. (2013). The primitive mantle value is from Sun and McDonough (1989); the depleted mantle value is from Salters and Stracke (2004). The dotted line represents the terrestrial magmatic array from Niu (2004).

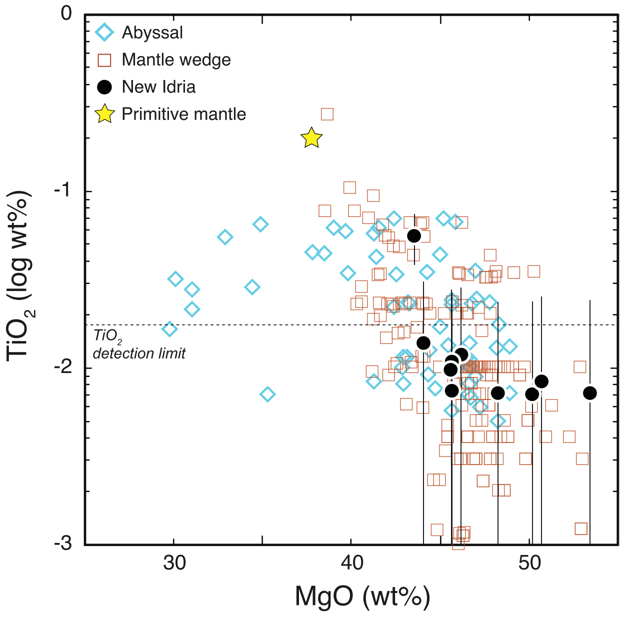

Fig. 6. TiO_2 versus MgO (wt%) for New Idria serpentinites and the global dataset of abyssal and mantle wedge serpentinites compiled in Deschamps et al. (2013). Primitive mantle from Sun and McDonough, 1989. The horizontal dashed line is the XRF detection limit for TiO_2, illustrating that most nominal TiO_2 values are effectively below detection.

that FME concentrations are decoupled from magmatic activity and are, therefore, more likely related to serpentinization by a slab-derived fluid.

The reasonably good correlation between Rb and Cs (Fig. 10a, $R^2 = 0.8$) suggests that both enrichments are related to the same process, likely serpentinization by a slab-derived fluid. In contrast, Ba and Cs are poorly correlated ($R^2 = 0.1$, Fig. 10b), which may indicate more than one fluid source that fractionates Ba from Cs and Rb. Given the partial overlap of Ba values with the global mantle wedge database (Figs. 7–10) and the well-established geochemical link between Ba enrichment and subduction-derived fluids (Deschamps et al., 2013; Peters et al., 2017), one of the Ba sources is likely to be the slab. The other source may be dispersed blocks of entrained Franciscan lithologies (Coleman, 1961), known to contain trace abundances of barite and other baric minerals, the most famous of which is benitoite ($BaTiSi_3O_9$): the official state gem of California (Van Baalen, 2004; Wise and Moller, 1995). If aqueous fluids leach Ba from Franciscan lithologies to the surrounding serpentinites, then this signal may be locally superimposed onto a slab-derived signal, resulting in poor Ba-Cs correlation and anomalously enriched Ba values in some specimens (Fig. 10b). This mobilization may be driven by redox effects in which the reduced conditions stabilized by serpentinization (Klein et al., 2013; Lazar, 2020) convert barite-hosted sulfate to sulfide, releasing Ba^{2+} to the local environment (see Section 5.3.4).

We conclude the FME discussion by ruling out mineralogical explanations for the observed LILE enrichments. Barite is associated with moderately high Ba in SP1B, but was not detected in any other rocks, including specimens with even higher Ba. The two rocks with the highest Ba (AM1 and SAM) contain secondary calcite (Fig. 4e), a sensible potential mineral host for alkaline metals, but N1R1C has similarly high Ba concentrations and no calcite or other suitable host phase. Cs and Rb might, in theory, be correlated to major or minor alkali element concentrations, but Na_2O and K_2O are detectable in only one sample, MM21, which features a Na-Ca amphibole (Fig. 4f). However, MM21 does not feature anomalously high LILE concentrations. Finally, no rock with high Cs or Rb also contained a K-bearing phase such as mica. Cs and Rb may instead be adsorbed onto serpentine itself in a manner that remains poorly understood (Lafay et al., 2016).

Most New Idria rocks contain the transition metal accessory assemblages awaruite (Ni_3Fe)–magnetite or awaruite–magnetite–heazlewoodite (Ni_3S_2), indicative of the low oxygen fugacity (fO_2) values typical in serpentinites in a variety of tectonic settings (Klein and Bach, 2009; Lazar, 2020). Three specimens did not contain awaruite (AM1, SAM, SP1B), suggesting slightly more oxidized conditions. Although LILEs are not themselves redox-sensitive, fO_2 is linked to the Fe^{2+}/Fe^{3+} ratio in major minerals such as serpentine (Andreani et al., 2013; Klein et al., 2013), which could affect coupled substitutions and, consequently, trace element partitioning. However, high-LILE and low-LILE specimens are found in both awaruite-bearing and awaruite-free rocks, so no straightforward correlation between fO_2 and whole-rock LILE concentration is apparent from the current study.

5.2.2. *U-Th systematics*

Although uranium can be a fluid-mobile element with behavior similar to Cs, Ba, and other LILEs, the following analysis of U-Th systematics indicates that U concentrations at New Idria are more likely to have resulted from a magmatic process. Whereas Th is predominantly fluid-immobile, uranium is mobilized by oxidizing fluids such as seawater, which leads to U enrichments of 2–3 orders of magnitude in abyssal serpentinites (Peters et al., 2017). In many mantle wedge serpentinites, U is enriched over Th by an order of magnitude or more due to the preferential partitioning of U in slab fluids. Such U-Th fractionation is not observed at New Idria, where U/Th ratios are consistent with a magmatic U/Th, averaging 0.31 ± 0.04 (1 s.d.) (Table 4) and within error of typical magmatic values for the depleted mantle, e.g., U/Th = 0.34 ± 30% (Salters and Stracke, 2004). Moreover, the low standard deviation of U/Th in the New Idria specimens reflects relatively constant values throughout suite. These constant, mantle-typical values are illustrated in a plot of U versus Th (Fig. 11) in which all specimens are well-correlated to the magmatic array that retains a U/Th signature of melt–rock interactions (Niu, 2004). Therefore, a fluid origin for U and Th is disfavored.

Melt–rock interaction can also explain the observed UTh systematics and decoupling of U from other fluid-mobilized LILEs at New Idria.

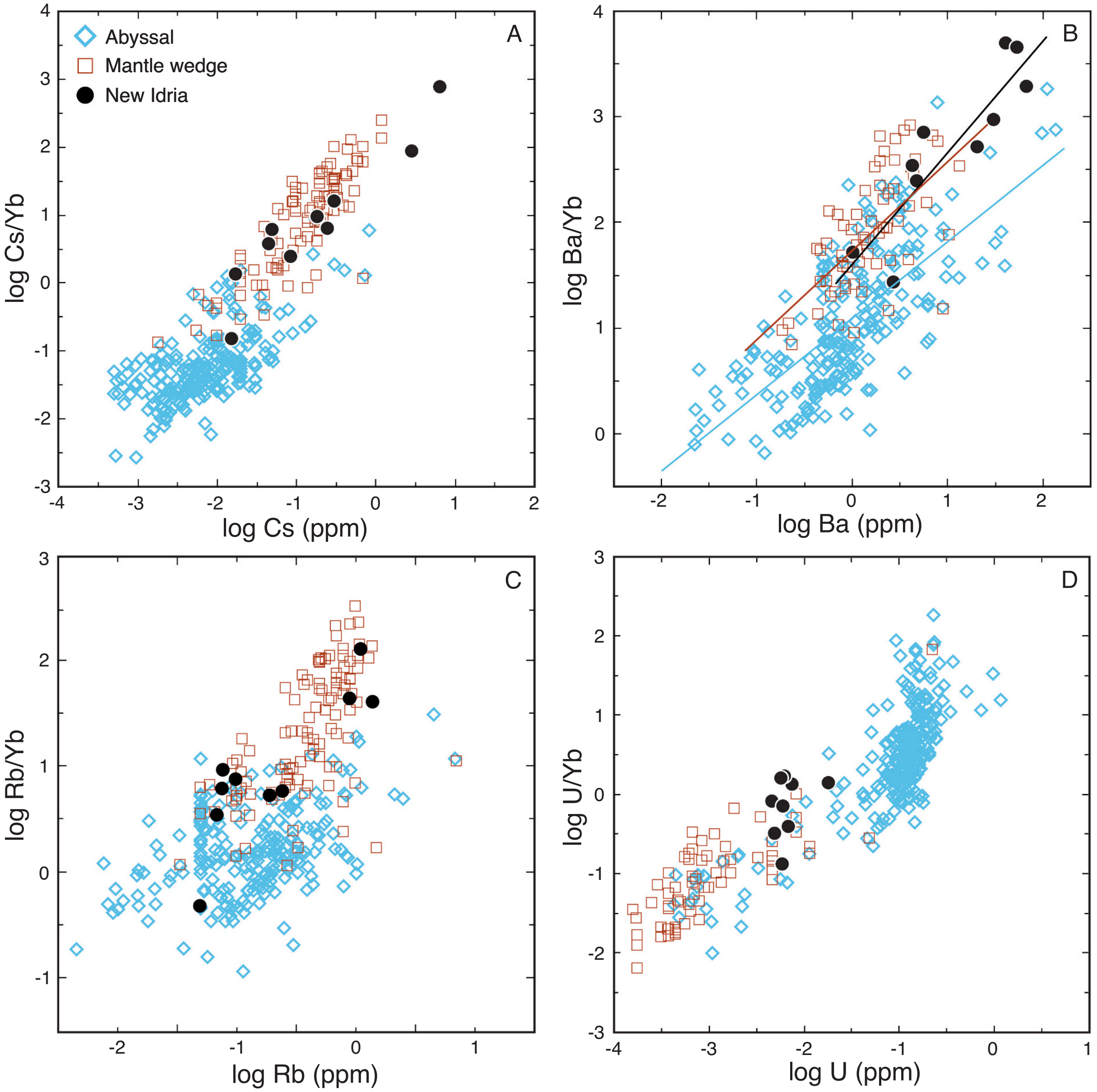

Fig. 7. Cs/Yb vs. Cs (*A*), Ba/Yb vs. Ba (*B*), Rb/Yb vs. Rb (*C*), and U/Yb vs. U (*D*) for New Idria compared to a global dataset of abyssal and mantle wedge serpentinites compiled by Peters et al. (2017).

Concentrations of fluid-mobile elements controlled by a single process should be generally correlated, as shown by the behavior of Rb and Cs in Fig. 10a. This correlation is absent in a plot of U vs. Cs (Fig. 10c), in which U values are comparatively constant over a Cs range of three orders of magnitude, indicating that the fluid processes that control Cs do not affect U. Enrichment due to melt–rock interaction also explains the differences in Yb-normalized behavior between U, Cs, and Ba. Values of Cs/Yb vs. Cs and Ba/Yb vs. Ba are well within the mantle wedge range, consistent with the influence of slab fluids (Figs. 7a–b). In contrast, U enrichment along the magmatic array can explain elevated, less tectonically distinct U/Yb vs. U values that are intermediate to the predominant mantle wedge and abyssal signatures (Fig. 7d).

5.2.3. HFSE

In general, high field strength elements are used to interpret the magmatic history of peridotitic protoliths because they are immobile during serpentinization and other aqueous processes (Deschamps et al., 2013; Kodolányi et al., 2012; Scambelluri et al., 2004). Therefore, we may apply certain HFSE discrimination diagrams traditionally used for igneous rocks to the interpretation of the New Idria serpentinites. A classic magmatic diagram, first developed by Pearce (1982), shows that arc-derived lavas retain Th/Yb and Ta/Yb values distinct from oceanic lavas such as mid-ocean ridge basalts (MORB) and ocean island basalts (OIB), owing to fractionation between Th and Ta in subduction systems. Mantle wedge serpentinites share these signatures: greater than 90% of all mantle wedge serpentinites with detectable Ta have Th/Yb and Ta/Yb values that fall within the arc-derived field described by Pearce (1982) (Fig. 12). This observation supports the idea that these elements are broadly conservative throughout melting and metamorphism. In contrast, the abyssal data are more widely distributed throughout Fig. 12, likely reflecting the high variability of Th and Ta in ocean floor serpentinites due to the tendency for HFSEs to be mobilized by seawater (Orians and Merrin, 2010). From this perspective, a mantle wedge origin for New Idria is favored over an abyssal origin based on the skewed distribution of the data toward the arc region of the diagram and on the absence of data on or below the MORB–OIB trend. Because these

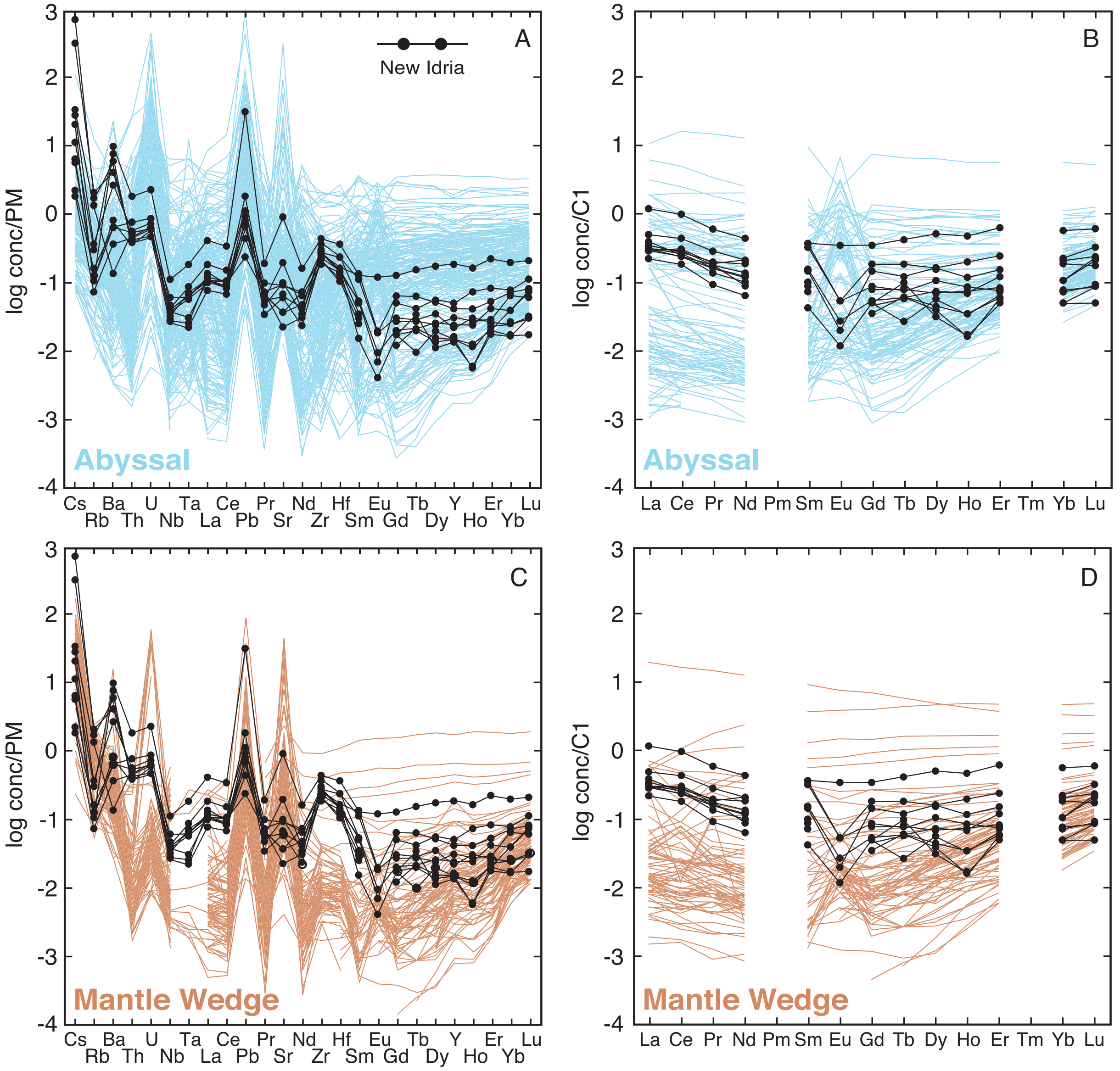

Fig. 8. Trace element (a and c) and rare earth element concentration (conc) diagrams (b and d) of New Idria serpentinites (black lines) compared to global abyssal (a, b) (blue) and mantle wedge (c, d) (orange) signatures compiled in Deschamps et al. (2013). Trace element concentrations are normalized to primitive mantle values (PM) (Sun and McDonough, 1989) and rare earth element data are normalized to C1 chondrite values (C1) (McDonough and Sun, 1995). The elements Pm and Tm are below detection in all specimens.

elements are fluid-immobile, this signature is likely related to melt–rock interactions.

Another magmatic HSFE relationship may be visualized in a plot of Hf/Nb versus Zr/Nb. Because Nb is preferentially partitioned into basaltic magma relative to Hf and Zr, partial melting favors increasing Hf/Nb and Zr/Nb ratios in the residual mantle, a relationship that has been previously shown to exist as a linear magmatic array in Vanuatu arc lavas (Sorbadere et al., 2013). A well-correlated linear relationship is similarly expressed in the global dataset of mantle wedge serpentinites ($R^2 = \sim 1.0$, brown symbols, Fig. 13). The minimal scatter about this linear trend suggests that magmatic source depletion is sufficient to explain most or all variations in Hf/Nb and Zr/Nb throughout the global mantle wedge dataset. In contrast, the global abyssal values are more variable ($R^2 = 0.6$, blue symbols, Fig. 13). This comparative scatter may be explained by seawater interactions on the ocean floor, which are known to mobilize HFSEs (Orians and Merrin, 2010). The New Idria data are not similarly scattered ($R^2 = 0.8$) and overlap the linear magmatic trend, favoring an origin in the mantle wedge. Moreover, the notably high Hf/Nb and Zr/Nb values relative to other mantle wedge serpentinites suggests that the New Idria protolith was extremely depleted mantle residue, consistent with the above interpretations based on major elements (Figs. 5 and 6).

5.2.4. REE

The REE data fall within a concentration range of 0.01–1 ppm (Figs. 8b and d) and show slightly elevated light rare earth element (LREE) concentrations relative to heavy rare earth elements (HREE), with 9 out of 10 specimens having La/Yb > 2 and as high as 9.5 (Table 4). Because LREEs are more incompatible during melting than HREEs, elevated LREE/HREE ratios could be explained by addition of basaltic melt to the protolith, noting that La/Yb in the primitive mantle is 1.4 (Sun and McDonough, 1989). Alternatively, because LREEs are more soluble in aqueous fluids than HREE, these REE ratios may reflect input from a fluid (Paulick et al., 2006). Discriminating between these

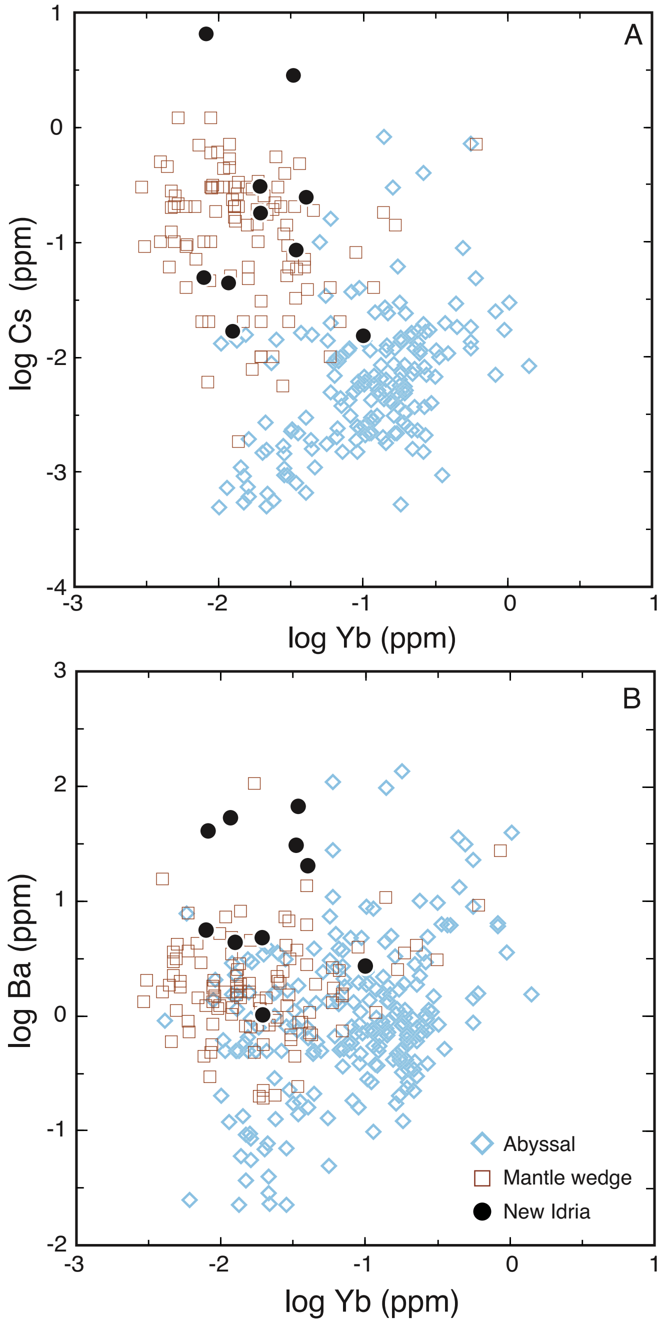

Fig. 9. Cs vs. Yb (*A*) and Ba vs. Yb (*B*) for New Idria compared to a global dataset of abyssal and mantle wedge serpentinites compiled by Peters et al. (2017).

two possibilities is enabled by plotting Nb vs La (Fig. 14) to represent relationships between HFSE elements (Nb) and LREEs (La). Arrows on the graphs illustrate trajectories for melt–rock interactions and fluid-–rock interactions (Paulick et al., 2006). The steeper, solid arrow represents a trajectory of melt–rock interaction, which is also aligned to the magmatic array (yellow symbols). The gently-sloped dashed vector represents fluid–rock interactions, reflective of the comparatively stronger partitioning of La into a fluid phase. The New Idria data is more consistent with the trajectory of melt–rock interaction, ruling out a fluid process to explain the REE behavior. Interpreting tectonic origin using the REE results is somewhat ambiguous, however, because the New Idria data fall along a trend that overlaps the abyssal dataset and a linear series of mantle wedge values.

5.3. Minerals

5.3.1. Chromite

Another indicator of the degree of partial melting is the chromium number (Cr#) of the chromite phase (Deschamps et al., 2013). Because Cr is refractory relative to Al during magmatic processes, Cr# in residual chromites generally increases as melt fraction increases, with the highest Cr# values occurring in the most depleted peridotites. Although there is some degree of overlap, abyssal samples tend to contain chromites with Cr# values in the range 0.2–0.6 and mantle wedge samples tend to contain chromites with Cr# values greater than 0.4, but often greater than 0.6 (Deschamps et al., 2013; Gamal El Dien et al., 2019). Seven out of 10 of the New Idria rocks have chromites with Cr# values from 0.57–0.83, which are more strongly associated with a mantle wedge signature. These results reproduce a previous chromite analysis in a New Idria serpentinite that yielded a Cr# of 0.64 (Yamada et al., 2019).

Some caution is advised in the interpretation that Cr# is a straightforward fingerprint for melt depletion because secondary metamorphic alteration of chromite may redistribute Cr and erase primary magmatic fingerprints (Gamal El Dien et al., 2019). Three New Idria rocks show textural evidence in support of such alteration. Sample RH8 contains chromites with significantly variable Cr# values, from 0.41 to 0.86, accompanied by conspicuous reaction microtextures (Fig. 4a) and elevated Cr in neighboring serpentine. Chromites in SP1B have the highest Cr# values, with minor spatial variations of ±7% (2sd) and reactive textures in contact with Cr-bearing chlorite and serpentine. Sample COL1 shows reactive intergrowth between chromite and Cr-andradite (Fig. 4b), with Cr# values that vary ±5% (2sd). On the other hand, samples AM1, N1R1C, and SM52 contain chromites with mantle wedge Cr# values of 0.65–0.74, but show no textural evidence for Cr redistribution: no detectable Cr in neighboring phases, spatially constant Cr# values within uncertainty, and no reactive textures other than the nucleation of magnetite rims ubiquitous to all specimens (Fig. 4c). If metasomatism or some similar process alters chromite compositions in New Idria serpentinites, not all rocks appear to be affected. Unaltered specimens retain Cr# values consistent with a mantle wedge origin.

5.3.2. Antigorite

The presence of antigorite is also indicative of serpentinization in the mantle wedge. Antigorite is generally considered to be the highest-grade serpentine mineral, stable above 300 °C and up to 80 kbar (Evans, 2004; Ulmer and Trommsdorff, 1995) and likely abundant in the serpentinized forearc mantle (Hyndman and Peacock, 2003). Previous reports of antigorite at New Idria in close proximity to eclogite and blueschist-grade metabasalts (Tsujimori et al., 2007) suggest similarly high-grade serpentinization, mirroring observations of antigorite in the Mariana forearc (Alt and Shanks III, 2006; Parkinson and Pearce, 1998). Therefore, the present observations of antigorite in specimens COL1, SM52, and SP1B may be interpreted to be consistent with the elevated P and T of the mantle wedge. These three documented occurrences may be an underestimate of antigorite abundance at New Idria because resolving antigorite via XRD is not as sensitive as Raman spectroscopy and because antigorite is often replaced by retrograde lizardite (Evans, 2004). On the other hand, small amounts of antigorite are occasionally reported in abyssal serpentinites (Debret et al., 2017; Klein et al., 2017), suggesting some caution with a definitive association of antigorite with subduction zones. Nevertheless, the presence of antigorite at New Idria in context with the preponderance of other evidence points to a high-grade origin consistent with the mantle wedge.

5.3.3. Sodic-calcic amphibole

The Na-Ca amphibole found in specimen MM21 (location F, Fig. 2) may be interpreted as a result of localized metasomatism based on several lines of evidence. First, no other specimen in the study contains a sodic phase of any kind, suggesting that the process responsible for

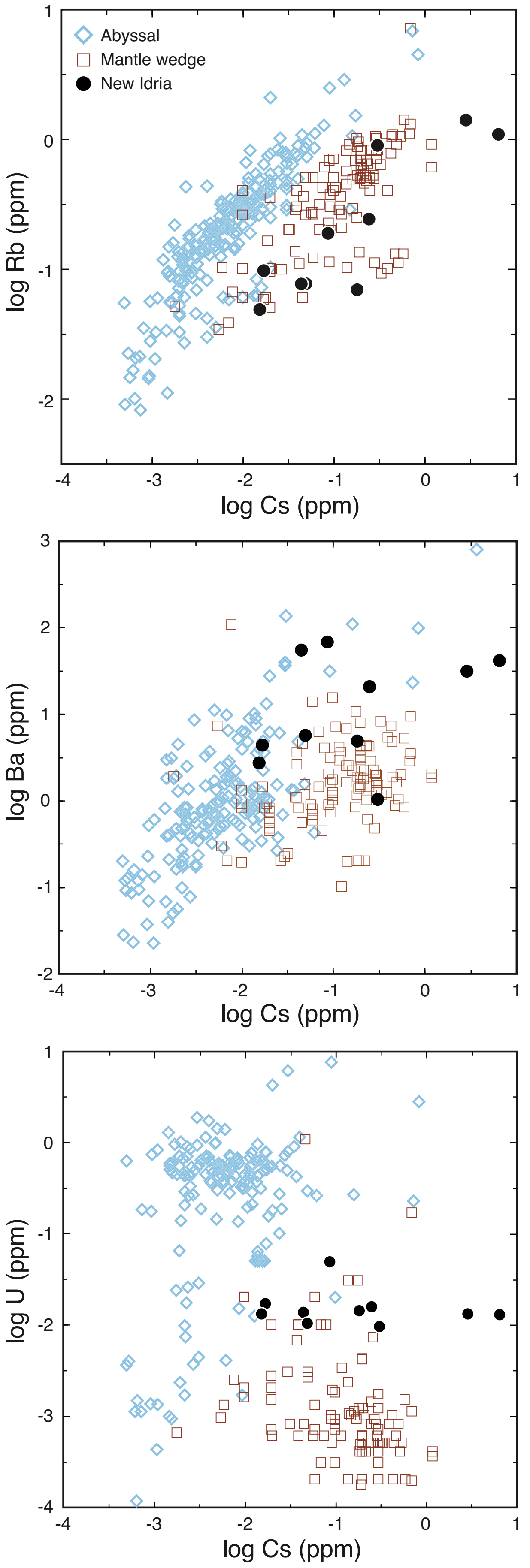

(caption on next column)

Fig. 10. Rb (*A*), Ba (*B*), and U (*C*) vs. Cs for New Idria compared to a global dataset of abyssal and mantle wedge serpentinites compiled by Peters et al. (2017).

stabilizing a sodic-calcic amphibole is limited to location F. Second, MM21 is located near documented exposures of a Miocene-aged (12–13 Ma) syenite (red dots, Fig. 2) composed predominantly of sodic feldspar and kaersutite, a sodic-calcic amphibole (Van Baalen, 2004). These sodic phases provide a straightforward source of Na, and amphibole saturation implies elevated H_2O activity. Together, these phases provide the components for a Na-bearing aqueous fluid emanating from the syenite intrusion. Third, textural relations revealed in a backscattered image of MM21 suggest infiltration of a sodic, oxidizing fluid along grain boundaries (Fig. 4f). The overall reflective appearance of the intergranular reaction zone is due to a concentration of Fe, which could have been oxidized and leached from olivine, serpentine, and/or pyroxene by the infiltrating fluid. Also, the sodic-calcic amphibole appears to replace pyroxene along the margin of this reactive zone. In summary, the singular occurrence of the sodic-calcic amphibole in close proximity to a syenite intrusion with textural evidence consistent with an infiltrating Na-rich, oxidizing fluid supports the interpretation this mineralization is a localized metasomatic event. Because Na-Ca amphiboles are often associated with blueschist-grade metamorphism (Spear, 1993), this inferred metasomatism may have occurred at elevated pressures relevant to the mantle wedge, although such an interpretation is speculative without further quantitative compositional analyses and a rigorous thermodynamic analysis.

5.3.4. *Barite*

The origin of barite in specimen SP1B is more difficult to constrain. Barite is rarely reported in serpentinites, and is apparently also rare at New Idria. We are aware of one other published barite occurrence in a serpentinite, reported in a subducted ophiolitic specimen from the Italian Alps (Evans et al., 2017). No previous study has systematically addressed this unusual association. A thermodynamic analysis is prevented at present by a lack of standard state free energy data for barite at pressures greater than 1400 bar (Blount, 1977), although indirect field evidence suggests that barite stability in serpentinites is insensitive to P and T over the range of metamorphic grades relevant to subduction. For example, barite has been reported over a notably wide range of P–T conditions from seafloor sediments and hydrothermal systems (Plank, 2013) to greenschist-grade metamorphism (Clark et al., 1999) to eclogitic-grade metamorphism (Wang et al., 2016). Also, diamond anvil cell experiments on $BaSO_4$ composition show that barite does not undergo a polymorphic transition until 100 kbar at 25 °C, with a positive Clapeyron slope that shifts to even higher pressures as temperature increases (Lee et al., 2001). Therefore, even if standard state thermodynamic data were available for equilibrium mineral–fluid stability calculations, it is unclear whether barite would provide useful geothermobarometric constraints.

Despite such ambiguities, some tentative inferences on the origin of barite in SP1B are possible, based on limited compositional and paragenetic constraints. First, as explained in Section 5.2.1, barite saturation appears to be independent of whole-rock Ba concentration because four other specimens are richer in Ba but we did not observe barite in them. Second, accessory mineral parageneses provide indirect evidence that barite stability in serpentinites is fO_2-dependent. This may be illustrated by the observations that the barite-bearing SP1B and Italian Alps (Evans et al., 2017) rocks contain awaruite-free accessory mineral assemblages: respectively, heazlewoodite–millerite–magnetite (Table 2) and pyrite–magnetite. Following the phase relations derived by Klein and Bach (2009) for 150–400 °C and 500 bar in the system Fe–Ni–S–O, both of these awaruite-free assemblages are several log fO_2 units more oxidizing than the corresponding awaruite-bearing assemblages present in other New Idria specimens, assuming minimal pressure effects on the

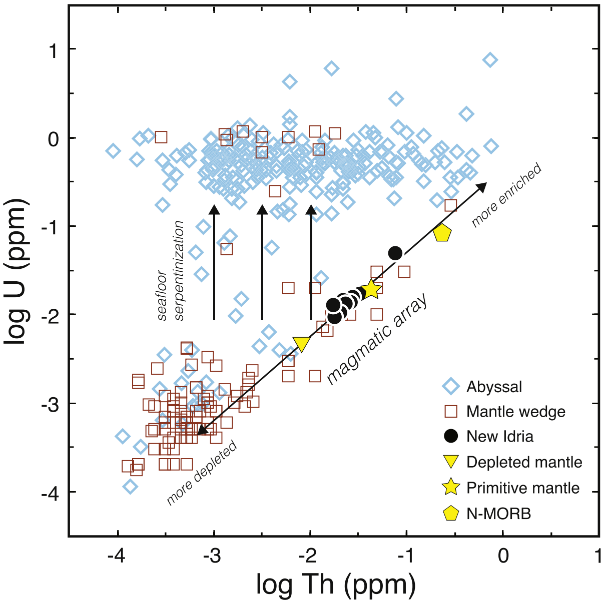

Fig. 11. U vs. Th for New Idria compared to a global dataset of abyssal and mantle wedge serpentinites compiled by Deschamps et al. (2013). Following Niu (2004), the diagonal melt–rock mixing line (double arrow) represents the effect of pre-serpentinization magmatic activity. Vertical arrows indicate the effect of U addition decoupled from Th via seafloor serpentinization. Primitive mantle from Sun and McDonough (1989); depleted mantle from Salters and Stracke (2004); N-MORB average from Gale et al. (2013).

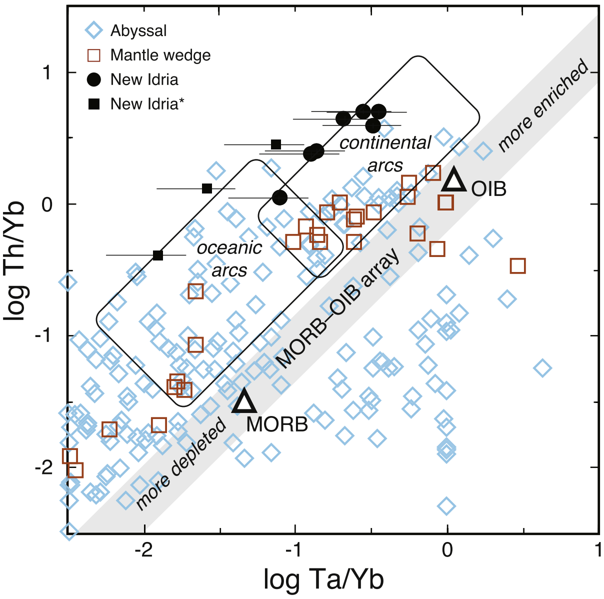

Fig. 12. Th/Yb vs. Ta/Yb for New Idria compared to a global dataset of abyssal and mantle wedge serpentinites compiled by Peters et al. (2017), following the igneous discrimination diagram of Pearce (1982). *Black squares have reported Ta concentrations at the detection limit. Average N-MORB value is from Gale et al. (2013); average OIB value is from Niu and O'Hara (2003). The gray area is the MORB–OIB magmatic mixing array. Oceanic and continental arc signatures are sketched from Pearce (1982).

corresponding equilibria. Therefore, barite appears to exist only in association with oxidized mineral assemblages, which implies that barite stability is redox sensitive. This implication is illustrated by the following barite–fluid equilibrium:

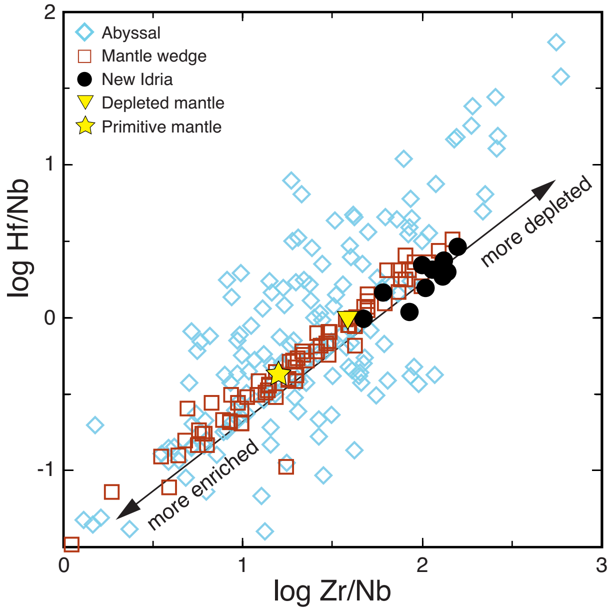

Fig. 13. Hf/Nb vs. Zr/Nb for New Idria compared to a global dataset of abyssal and mantle wedge serpentinites compiled by Peters et al. (2017). Primitive mantle from Sun and McDonough (1989); depleted mantle from Salters and Stracke (2004). Double arrow is a magmatic mixing array.

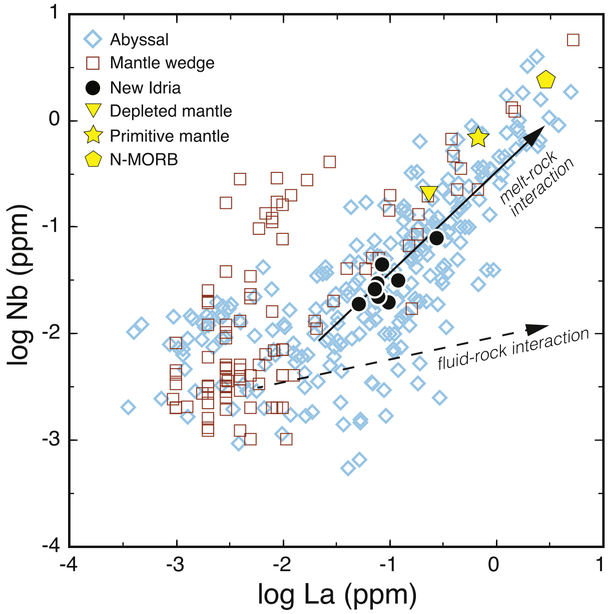

Fig. 14. Nb vs. La for New Idria compared to a global dataset of abyssal, mantle wedge, and subducted serpentinites compiled by Peters et al. (2017). Primitive mantle from Sun and McDonough (1989); depleted mantle from Salters and Stracke (2004); N-MORB average from Gale et al. (2013). Solid line represents the enrichment trend following melt–rock interaction; Dashed line represents the enrichment trend following fluid–rock interaction.

$$BaSO_{4(\mathrm{barite})} + 2H_2O \Leftrightarrow H_2S + Ba^{2+} + 2OH^{-} + 2O_2$$

where decreasing fO_2 would cause a shift toward the right, leading to dissolution or destabilization of barite in favor of sulfide. Similar systematics have been described for other nonsilicate oxyanionic minerals such as anhydrite (Newton and Manning, 2005) and calcite (Lazar et al., 2014) in which fO_2-buffered aqueous experiments and calculations show that decreased oxygen fugacity favors destabilization and/or increased solubility.

5.4. *Implications*

Multiple lines of evidence support an origin of the New Idria serpentinite diapir in the mantle wedge. Previous authors inferred a deep origin based on the association of isolated entrained blueschist- and eclogite-grade blocks that record pressures of 10–13 kbar and boron isotope signatures consistent with slab-derived fluids within the serpentinite (Coleman, 1961; Takahashi et al., 2018; Tsujimori et al., 2007). Here, we present several lines of evidence for a deep origin of the New Idria serpentinite based on bulk rock geochemistry and petrography of the serpentinites. First, several geochemical signatures suggest that the protolith of the New Idria suite was a highly depleted peridotite, as would be expected in the high melt flux setting of the mantle wedge. Major element relationships show depleted TiO_2 and enriched MgO, high MgO/Al_2O_3 and low Al_2O_3/SiO_2, and Cr-rich chromites. Notably high Hf/Nb and Zr/Nb ratios revealed HSFE systematics consistent with a highly depleted source that are also well-correlated to the global mantle wedge dataset.

Second, the influence of a slab-derived fluid is supported by enriched FME concentrations in some of the most Cs-rich and Ba-rich serpentinites ever reported. The well-established link between Cs and Ba enrichment and slab-derived fluids suggests that these serpentinites were hydrated at depth along or near the slab–mantle interface. For the most Cs-rich rock, N1R1C, one of the more convincing observations is its unremarkable petrography as a “normal” serpentinite, with no evidence for subsequent metasomatic alteration nor infiltrated melt, and no observations of an exotic Cs-bearing phase (Fig. 4c and Table 2). Also, N1R1C is not located near any known outcrops of tectonic blocks or other non-serpentinite lithologies, Franciscan or otherwise, suggesting the absence of a suitable Cs source. Therefore, the simplest explanation for the high Cs in the rock is primary serpentinization by a Cs-rich fluid sourced from the deep subducted slab. Moreover, Cs, Ba, and Rb values for New Idria are consistent with the global mantle wedge database, although some Ba signals are anomalously high and may be partly sourced locally by dissolution of baric minerals in isolated, dispersed Franciscan blocks.

Finally, the behaviors of some incompatible elements are consistent with melt-rock interactions that are difficult to explain in an abyssal setting. The elevated U and Th values are well-resolved from abyssal signatures and lie along a trend consistent with magmatic fractionation. Values for Th/Yb and Ta/Yb are more consistent with an arc-derived magmatic signature that is broadly shared by the global mantle wedge database, and poorly correlated to the high variability of global abyssal serpentinites.

Together, these lines of evidence may be synthesized into the petrogenetic interpretation that the New Idria represents a highly depleted mantle wedge overprinted by melt–rock interaction and serpentinized by slab-derived fluids. This serpentinization would have been at considerable depth, as implied by the low Rb/Cs ratios and the presence of antigorite. Moreover, one serpentinite, MM21, contains Na-Ca amphibole which may indicate local metasomatism at blueschist-grade conditions, consistent with the reports of metabasaltic tectonic inclusions by Tsujimori et al. (2007) near this sample.

A similar multi-step geochemical fingerprint has also been proposed for Tso Morari, a forearc serpentinite massif in the Himalayan Indus Suture Zone (Deschamps et al., 2010). Though not a diapiric structure, the Tso Morari data suggest that the geochemical processes operating at New Idria may not be specific to central California. In context with serpentinites in the Franciscan Complex, the slab signature is most similar to FME-rich rocks found in the Redwood City serpentine mélange, also proposed to originate from the mantle wedge, though lacking evidence for melt re-fertilization (Uno and Kirby, 2019). Many other Franciscan deposits contain abyssal signatures (Barnes et al., 2013), suggesting regional diversity in serpentinite petrogenesis.

On a final note, the forearc serpentinite diapir hypothesis implies the existence of a mantle wedge, which in turn requires a subduction zone. Upwelling of serpentinite along the Mariana forearc has a straightforward correlation to the active subduction of the Pacific Plate, but tectonic convergence in central California ceased around 25 Ma (Wakabayashi, 2015; Wallace, 1990). Therefore, if New Idria is derived from mantle wedge, it is likely to be an excavation of remnant mantle wedge serpentinized millions of years ago during the final stages of Farallon plate subduction. Delayed release of mantle wedge serpentinite is consistent with a recent seismic tomography study that imaged an isolated 100 km-wide high-velocity zone bordering the eastern margin of New Idria (Wang et al., 2013). This zone, called the Isabella anomaly, has been interpreted to be an unsubducted fossil slab: a subsurface microplate fragment of the Farallon plate frozen in place. The existence of New Idria in its current location may indicate that this fossil slab is (or was) overlain by forearc mantle wedge, implying a plausible source for a serpentinite diapir hydrated along a slab–mantle interface. The fact that no other fossil slab anomalies have been discovered along the entire length of the San Andreas fault may explain why large serpentinite diapirs on the scale of New Idria are not found elsewhere in California, in contrast to the chain of numerous submarine diapiric seamounts found along the Mariana forearc (Fryer et al., 1999).

The delayed timing of diapiric rise from an extinct slab–mantle interface is reasonable to a first order given current tectonic and geodynamic constraints. Petrographic analyses of the metabasalt tectonic blocks entrained in New Idria yielded minimum pressures of 8–13 kbar (Tsujimori et al., 2007). Adopting the value of 13 kbar and an approximate lithostatic pressure gradient of 3.5 km/kbar, an approximate slab–mantle interface depth may be calculated to be ~45 km. Detrital thermochronology of serpentinite sediments in the Big Blue formation, presumed to erode from New Idria, show ages as young as ~14 Ma, indicating an 11-million-year lag time, at most, between the end of subduction and the emergence of a diapir at New Idria. The uplift rate of New Idria has been estimated to be 4 mm/year (Coleman, 1996; Tsujimori et al., 2007); therefore, 11 million years of diapiric rise would result in a travel distance of 44 km, on par with the estimated slab–mantle interface depth. Uplift may have been aided by release of water from the slab (Uno and Kirby, 2019) and/or may have exploited weaknesses along the San Andreas fault system (Guillot et al., 2015). Regardless of the uplift mechanism, the geochemical signatures presented in this study support the hypothesis that the ultimate origin of the New Idria serpentinite body is hydration of the mantle wedge by slab-derived fluids.

6. Conclusions

We present mineralogical and whole-rock geochemical data for the New Idria serpentinite body in central California. The results have been interpreted to reflect three petrogenetic processes which support the hypothesis that the New Idria body is a diapiric fragment of mantle wedge serpentinized at depth. First, a highly depleted protolith consistent with a mantle wedge origin is inferred from high MgO/SiO_2 and low Al_2O_3/SiO_2, low TiO_2, Cr-rich chromites, elevated Th and Ta relative to Yb, and notably enriched $HFSE^{+4}/HFSE^{5+}$ ratios. Second, plots of U vs. Th and Nb vs. Ta reveal covariant values that lie along melt-rock interaction vectors, suggesting melt re-fertilization of the protolith prior to serpentinization. Finally, highly enriched Cs and Ba, and to a lesser extent Rb, are interpreted to be derived from serpentinizing FME-rich fluids emerging from a subducted slab. In aggregate, these data suggest that the New Idria serpentinite body is a mantle wedge remnant from the final stages of subduction of the Farallon Plate during the Miocene, a tectonic interpretation broadly consistent with independent evidence from a variety of geodynamic, geophysical, and petrological studies. This implies that New Idria may represent a continental analog to the submarine serpentine mud volcanoes along the Mariana forearc, albeit emergent from a recently extinct subduction zone.

Declaration of Competing Interest

The authors declare that they have no known competing financial interests or personal relationships that could have appeared to influence the work reported in this paper.

Acknowledgments

This paper is dedicated to the memory of Dr. Robert Coleman for his foundational work on New Idria in the mid-20th century and thereafter. The authors greatly appreciate constructive reviews by Daniel Peters and Ivan Savov and editorial handling by Marco Scambelluri. Thanks to Ashley Steiner and Arron Steiner of the Washington State University GeoAnalytical Lab. Special thanks to the CSUSB Advanced Field Geology undergraduate students who helped collect and curate some of the specimens analyzed in this study: Michael Murrey, Silvia Flores, Hannah Shields, David Williams, and Joy Berry. Funding for this project was provided by a University of Southern California faculty startup grant (Cooperdock) and a CSUSB PRISM grant (Lazar).

Appendix A. Supplementary data

Supplementary data to this article can be found online at https://doi.org/10.1016/j.lithos.2021.106252.

References

Albers, E., Kahl, W.-A., Beyer, L., Bach, W., 2020. Variant across-forearc compositions of slab-fluids recorded by serpentinites: implications on the mobilization of FMEs from an active subduction zone (Mariana forearc). Lithos 364, 105525. https://doi.org/10.1016/j.lithos.2020.105525.

Alt, J., Shanks III, W., 2006. Stable isotope compositions of serpentinite seamounts in the Mariana forearc: serpentinization processes, fluid sources and sulfur metasomatism. Earth Planet. Sci. Lett. 242 (3–4), 272–285. https://doi.org/10.1016/j.epsl.2005.11.063.

Andreani, M., Muñoz, M., Marcaillou, C., Delacour, A., 2013. µXANES study of iron redox state in serpentine during oceanic serpentinization. Lithos 178, 70–83. https://doi.org/10.1016/j.lithos.2013.04.008.

Atwater, B.F., Trumm, D.A., Tinsley, J.C.I., Stein, R.S., Tucker, A.B., Donahue, D.J., Jull, A.J.T., Payen, L.A., 1990. Alluvial plains and earthquake recurrence at the Coalinga anticline. U.S. Geol. Surv. Prof. Pap. 1487, 273–297.

Barnes, J.D., Eldam, R., Lee, C.-T.A., Errico, J.C., Loewy, S., Cisneros, M., 2013. Petrogenesis of serpentinites from the Franciscan Complex, western California, USA. Lithos 178, 143–157. https://doi.org/10.1016/j.lithos.2012.12.018.

Blount, C.W., 1977. Barite solubilities and thermodynamic quantities up to 300 °C and 1400 bars. Am. Mineral. 62, 942–957.

Bonatti, E., 1976. Serpentinite protrusions in the oceanic crust. Earth Planet. Sci. Lett. 32, 107–113. https://doi.org/10.1016/0012-821X(76)90048-0.

Clark, S.H.B., Gray, K.J., Back, J.M., 1999. Geology of the Barite Hill gold–silver deposit in the southern Carolina slate belt. Econ. Geol. 94 (8), 1329–1346. https://doi.org/10.2113/gsecongeo.94.8.1329.

Coleman, R.G., 1961. Jadeite deposits of the Clear Creek area, New Idria district, San Benito County, California. J. Petrol. 2, 209–247. https://doi.org/10.1093/petrology/2.2.209.

Coleman, R.G., 1996. New Idria serpentinite: a land management dilemma. Environ. Eng. Geosci. II (1), 9–22. https://doi.org/10.2113/gseegeosci.ii.1.9.

Cooperdock, E.H.G., Raia, N.H., Barnes, J.D., Stockli, D.F., Schwarzenbach, E.M., 2018. Tectonic origin of serpentinites on Syros, Greece: geochemical signatures of abyssal origin preserved in a HP/LT subduction complex. Lithos 296–299, 352–364. https://doi.org/10.1016/j.lithos.2017.10.020.

Cowan, D.S., Mansfield, C.F., 1970. Serpentinite flows on Joaquin Ridge, southern Coast Ranges, California. GSA Bull. 81, 2615–2628. https://doi.org/10.1130/0016-7606(1970)81[2615:SFOJRS]2.0.CO;2.

Debret, B., Andreani, M., Delacour, A., Rouméjon, S., Trcera, N., Edinburgh Ion Microprobe Facility, E, Williams, H., 2017. Assessing sulfur redox state and distribution in abyssal serpentinites using XANES spectroscopy. Earth Planet. Sci. Lett. 466, 1–11. https://doi.org/10.1016/j.epsl.2017.02.029.

Deschamps, F., Guillot, S., Godard, M., Chauvel, C., Andreani, M., Hattori, K., 2010. In situ characterization of serpentinites from forearc mantle wedges: timing of serpentinization and behavior of fluid-mobile elements in subduction zones. Chem. Geol. 269, 262–277. https://doi.org/10.1016/j.chemgeo.2009.10.002.

Deschamps, F., Guillot, S., Godard, M., Andreani, M., Hattori, K., 2011. Serpentinites act as sponges for fluid-mobile elements in abyssal and subduction zone environments. Terra Nova 23, 171–178. https://doi.org/10.1111/j.1365-3121.2011.00995.x.

Deschamps, F., Godard, M., Guillot, S., Hattori, K., 2013. Geochemistry of subduction zone serpentinites: a review. Lithos 178, 96–127. https://doi.org/10.1016/j.lithos.2013.05.019.

Ernst, W.G., 2016. Franciscan mélanges: coherent blocks in a low-density, ductile matrix. Int. Geol. Rev. 58, 626–642. https://doi.org/10.1080/00206814.2015.1108879.

Evans, B.W., 2004. The serpentinite multisystem revisited: chrysotile is metastable. Int. Geol. Rev. 46 (6), 479–506. https://doi.org/10.2747/0020-6814.46.6.479.

Evans, K.A., Reddy, S.M., Tomkins, A.G., Crossley, R.J., Frost, B.R., 2017. Effects of geodynamic setting on the redox state of fluids released by subducted mantle lithosphere. Lithos 278–281, 26–42. https://doi.org/10.1016/j.lithos.2016.12.023.

Fryer, P., Wheat, C.G., Mottl, M.J., 1999. Mariana blueschist mud volcanism: implications for conditions within the subduction zone. Geology 27, 103–106. https://doi.org/10.1130/0091-7613(1999)027<0103:MBMVIF>2.3.CO;2.

Gale, A., Dalton, C.A., Langmuir, C.H., Su, Y., Schilling, J.-G., 2013. The mean composition of ocean ridge basalts. Geochem. Geophys. Geosyst. 14, 489–518. https://doi.org/10.1029/2012GC004334.

Gamal El Dien, H., Arai, S., Doucet, L.-S., Li, Z.-X., Kil, Y., Fougerouse, D., Reddy, S.M., Saxey, D.W., Hamdy, M., 2019. Cr-spinel records metasomatism not petrogenesis of mantle rocks. Nat. Commun. 10, 5103. https://doi.org/10.1038/s41467-019-13117-1.

Guillot, S., Schwartz, S., Reynard, B., Agard, P., Prigent, C., 2015. Tectonic significance of serpentinites. Tectonophysics 646, 1–19. https://doi.org/10.1016/j.tecto.2015.01.020.

Hyndman, R.D., Peacock, S.M., 2003. Serpentinization of the forearc mantle. Earth Planet. Sci. Lett. 212, 417–432. https://doi.org/10.1016/S0012-821X(03)00263-2.

Johnson, D., Hooper, P., Conrey, R., 1999. XRF analysis of rocks and minerals for major and trace elements on a single low dilution Li-tetraborate fused bead. Adv. X-ray Anal. 41, 843–867.

Kawahara, H., Endo, S., Wallis, S.R., Nagaya, T., Mori, H., Asahara, Y., 2016. Brucite as an important phase of the shallow mantle wedge: evidence from the Shiraga unit of the Sanbagawa subduction zone, SW Japan. Lithos 254–255, 53–66. https://doi.org/10.1016/j.lithos.2016.02.022.

Klein, F., Bach, W., 2009. Fe–Ni–Co–O–S phase relations in peridotite–seawater interactions. J. Petrol. 50, 37–59. https://doi.org/10.1093/petrology/egn071.

Klein, F., Bach, W., McCollom, T.M., 2013. Compositional controls on hydrogen generation during serpentinization of ultramafic rocks. Lithos 178, 55–69. https://doi.org/10.1016/j.lithos.2013.03.008.

Klein, F., Marschall, H.R., Bowring, S.A., Humphris, S.E., Horning, G., 2017. Mid-ocean ridge serpentinite in the Puerto Rico Trench: from seafloor spreading to subduction. J. Petrol. 58 (9), 1729–1754. https://doi.org/10.1093/petrology/egx071.

Knaack, C., Cornelius, S., Hooper, P., 1994. Trace Element Analyses of Rocks and Minerals by ICP-MS. Open File Report. Washington State University.

Kodolányi, J., Pettke, T., Spandler, C., Kamber, B.S., Gméling, K., 2012. Geochemistry of ocean floor and fore-arc serpentinites: constraints on the ultramafic input to subduction zones. J. Petrol. 53, 235–270. https://doi.org/10.1093/petrology/egr058.

Lafay, R., Montes-Hernandez, G., Janots, E., Munoz, M., Auzende, A.L., Gehin, A., Chiriac, R., Proux, O., 2016. Experimental investigation of As, Sb and Cs behavior during olivine serpentinization in hydrothermal alkaline systems. Geochim. Cosmochim. Acta 179, 177–202. https://doi.org/10.1016/j.gca.2016.02.014.

Lazar, C., 2020. Using silica activity to model redox-dependent fluid compositions in serpentinites from 100–700 °C and 1–20 kbar. J. Petrol. 61 (11−12) https://doi.org/10.1093/petrology/egaa101.

Lazar, C., McCollom, T.M., Manning, C.E., 2012. Abiogenic methanogenesis during experimental komatiite serpentinization: implications for the evolution of the early Precambrian atmosphere. Chem. Geol. 326–327, 102–112. https://doi.org/10.1016/j.chemgeo.2012.07.019.

Lazar, C., Zhang, C., Manning, C.E., Mysen, B.O., 2014. Redox effects on calcite–portlandite–fluid equilibria at forearc conditions: carbon mobility, methanogenesis, and reduction melting of calcite. Am. Mineral. 99, 1604–1615. https://doi.org/10.2138/am.2014.4696.

Le Roux, V., Dick, H.J.B., Shimizu, N., 2014. Tracking flux melting and melt percolation in supra-subduction peridotites (Josephine ophiolite, USA). Contrib. Mineral. Petrol. 168, 1064. https://doi.org/10.1007/s00410-014-1064-9.

Lee, P.L., Huang, E., Yu, S.C., 2001. Phase diagram and equations of state of BaSO4. High Pressure Res. 21 (2), 67–77. https://doi.org/10.1080/08957950108201005.

Malvoisin, B., 2015. Mass transfer in the oceanic lithosphere: Serpentinization is not isochemical. Earth Planet. Sci. Lett. 430, 75–85. https://doi.org/10.1016/j.epsl.2015.07.043.

Martin, C., Flores, K.E., Harlow, G.E., 2016. Boron isotopic discrimination for subduction-related serpentinites. Geology 44 (11), 899–902. https://doi.org/10.1130/G38102.1.

McDonough, W.F., Sun, S.S., 1995. The composition of the earth. Chem. Geol. 120, 223–253. https://doi.org/10.1016/0009-2541(94)00140-4.

Murata, K., Maekawa, H., Yokose, H., Yamamota, K., Fujioka, K., Ishii, T., et al., 2009. Significance of serpentinization of wedge mantle peridotites beneath Mariana forearc, western Pacific. Geosphere 5 (2), 90–104. https://doi.org/10.1130/GES00213.1.

Nagaishi, K., Ishikawa, T., 2009. A simple method for the precise determination of boron, zirconium, niobium, hafnium and tantalum using ICP-MS and new results for rock reference samples. Geochem. J. 43 (2), 133–141. https://doi.org/10.2343/geochemj.1.0010.

Newton, R.C., Manning, C.E., 2005. Solubility of anhydrite, $CaSO_4$, in NaCl–H_2O solutions at high pressures and temperatures: applications to fluid–rock interaction. J. Petrol. 46, 701–716. https://doi.org/10.1093/petrology/egh094.

Niu, Y., 2004. Bulk-rock major and trace element compositions of abyssal peridotites: implications for mantle melting, melt extraction and post-melting processes beneath mid-ocean Ridges. J. Petrol. 45, 2423–2458. https://doi.org/10.1093/petrology/egh068.

Niu, Y., O'Hara, M.J., 2003. Origin of ocean island basalts: a new perspective from petrology, geochemistry, and mineral physics considerations. J. Geophys. Res. 108, 2209. https://doi.org/10.1029/2002JB002048.

O'Hanley, D.S., 1996. Serpentinites: Records of Tectonic and Petrological History, Oxford Monographs on Geology and Geophysics, 34. Oxford University Press, New York.

Orians, K.J., Merrin, C.L., 2010. Refractory metals. In: Turekian, K.K. (Ed.), Marine Chemistry & Geochemistry: A Derivative of Encyclopedia of Ocean Sciences, 2nd edition. Academic Press, Elsevier.

Parkinson, I.J., Pearce, J.A., 1998. Peridotites from the Izu–Bonin–Mariana forearc (ODP Leg 125): evidence for mantle melting and melt–mantle interaction in a supra-subduction zone setting. J. Petrol. 39 (9), 1577–1618. https://doi.org/10.1093/petroj/39.9.1577.

Paulick, H., Bach, W., Godard, M., De Hoog, J.C.M., Suhr, G., Harvey, J., 2006. Geochemistry of abyssal peridotites (Mid-Atlantic Ridge, 15°20′N, ODP Leg 209): implications for fluid/rock interaction in slow spreading environments. Chem. Geol. 234 (3–4), 179–210. https://doi.org/10.1016/j.chemgeo.2006.04.011.

Pearce, J.A., 1982. Trace element characteristics of lavas from destructive plate boundaries. In: Thorpe, R.S. (Ed.), Andesites. John Wiley & Sons, New York, pp. 525–548.

Peters, D., Bretscher, A., John, T., Scambelluri, M., Pettke, T., 2017. Fluid-mobile elements in serpentinites: constraints on serpentinisation environments and element cycling in subduction zones. Chem. Geol. 466, 654–666. https://doi.org/10.1016/j.chemgeo.2017.07.017.

Plank, T., 2013. The Chemical Composition of Subducting Sediments. In: Holland, H.D., Turekian, K.K. (Eds.), Treatise on Geochemistry, , Second editionvol. 4. Elsevier, Oxford, pp. 607–629. https://doi.org/10.1016/B978-0-08-095975-7.00319-3.

Polonia, A., Torelli, L., Gasperini, L., Cocchi, L., Muccini, F., Bonatti, E., Hensen, C., Schmidt, M., Romano, S., Artoni, A., Carlini, M., 2017. Lower plate serpentinite diapirism in the Calabrian Arc subduction complex. Nat. Commun. 8, 1–13. https://doi.org/10.1038/s41467-017-02273-x.

Salters, V.J.M., Stracke, A., 2004. Composition of the depleted mantle. Geochem. Geophys. Geosyst. 5, Q05B07 https://doi.org/10.1029/2003GC000597.

Savov, I.P., Ryan, J.G., D'Antonio, M., Kelley, K., Mattie, P., 2005. Geochemistry of serpentinized peridotites from the Mariana Forearc Conical Seamount, ODP Leg 125: implications for the elemental recycling at subduction zones. Geochem. Geophys. Geosyst. 6, Q04J15 https://doi.org/10.1029/2004GC000777.

Scambelluri, M., Fiebig, J., Malaspina, N., Müntener, O., Pettke, T., 2004. Serpentinite subduction: implications for fluid processes and trace-element recycling. Int. Geol. Rev. 46, 595–613. https://doi.org/10.2747/0020-6814.46.7.595.

Schuiling, R.D., 2011. Troodos: a giant serpentinite diapir. Int. J. Geosci. 2 (2), 98–101. https://doi.org/10.4236/ijg.2011.22010.

Shervais, J.W., Choi, S.H., Sharp, W.D., Ross, J., Zoglman-Schuman, M., Mukasa, S.B., 2011. Serpentinite matrix mélange: implications of mixed provenance for mélange formation. In: Wakabayashi, J., Dilek, Y. (Eds.), Mélanges: Processes of Formation and Societal Significance. Geological Society of America. https://doi.org/10.1130/2011.2480(01).

Snoke, A.W., Barnes, C.G., 2006. The development of tectonic concepts for the Klamath Mountains province, California and Oregon. In: Snoke, A.W., Barnes, C.G. (Eds.), Geological Studies in the Klamath Mountains Province, California and Oregon: A Volume in Honor of William P. Irwin. Geological Society of America. https://doi.org/10.1130/2006.2410(01).

Snow, J.E., Dick, H.J.B., 1995. Pervasive magnesium loss by marine weathering of peridotite. Geochim. Cosmochim. Acta 59 (2), 4219–4235. https://doi.org/10.1016/0016-7037(95)00239-V.

Sorbadere, F., Schiano, P., Métrich, N., Bertagnini, A., 2013. Small-scale coexistence of island-arc- and enriched-MORB-type basalts in the central Vanuatu arc. Contrib. Mineral. Petrol. 166 (5), 1305–1321. https://doi.org/10.1007/s00410-013-0928-8.

Spear, F.S., 1993. Metamorphic Phase Equilibria and Pressure-temperature-time-paths. Mineralogical Society of America, Washington DC.

Sun, S.S., McDonough, W.F., 1989. Chemical and isotopic systematics of oceanic basalts: implications for mantle composition and processes. Geol. Soc. Lond. Spec. Publ. 42 (1), 313–345. https://doi.org/10.1144/GSL.SP.1989.042.01.19.

Syracuse, E.M., van Keken, P.E., Abers, G.A., 2010. The global range of subduction zone thermal models. Phys. Earth Planet. Inter. 183, 73–90. https://doi.org/10.1016/j.pepi.2010.02.004.

Takahashi, N., Tsujimori, T., Chang, Q., Kimura, J.-I., 2018. In-situ lithium isotope geochemistry for a veined jadeitite from the New Idria serpentinite body, California: constraints on slab-derived fluid and fluid–rock interaction. Lithos 318–319, 376–385. https://doi.org/10.1016/j.lithos.2018.08.015.

Tsujimori, T., Liou, J.G., Coleman, R.G., 2007. Finding of high-grade tectonic blocks from the New Idria serpentinite body, Diablo Range, California: petrologic constraints on the tectonic evolution of an active serpentinite diapir. In: Convergent Margin Terranes and Associated Regions: A Tribute to W.G. Ernst. Geological Society of America. https://doi.org/10.1130/2007.2419(03).

Ulmer, P., Trommsdorff, V., 1995. Serpentine stability to mantle depths and subduction-related magmatism. Science 268 (5212), 858–861. https://doi.org/10.1126/science.268.5212.858.

Uno, M., Kirby, S., 2019. Evidence for multiple stages of serpentinization from the mantle through the crust in the Redwood City Serpentinite mélange along the San Andreas Fault in California. Lithos 336–337, 276–292. https://doi.org/10.1016/j.lithos.2019.02.005.

Van Baalen, M.R., 1995. The New Idria Serpentinite. Ph.D. dissertation. Harvard University (482 pp.).

Van Baalen, M.R., 2004. Migration of the Mendocino Triple Junction and the origin of titanium-rich mineral suites at New Idria, California. Int. Geol. Rev. 46, 671–692. https://doi.org/10.2747/0020-6814.46.8.671.

Vermeesch, P., Miller, D.D., Graham, S.A., De Grave, J., McWilliams, M.O., 2006. Multimethod detrital thermochronology of the Great Valley Group near New Idria, California. Geol. Soc. Am. Bull. 118 (1–2), 210–218. https://doi.org/10.1130/B25797.1.

Wakabayashi, J., 2015. Anatomy of a subduction complex: architecture of the Franciscan Complex, California, at multiple length and time scales. Int. Geol. Rev. 57, 669–746. https://doi.org/10.1080/00206814.2014.998728.

Wakabayashi, J., 2017. Serpentinites and serpentinites: Variety of origins and emplacement mechanisms of serpentinite bodies in the California Cordillera. Island Arc 26, e12205. https://doi.org/10.1111/iar.12205.

Wallace, R.E., 1990. The San Andreas Fault System, California. USGS Professional Paper 1515. https://doi.org/10.3133/pp1515.

Wang, Y., Forsyth, D.W., Rau, C.J., Carriero, N., Schmandt, B., Gaherty, J.B., Savage, B., 2013. Fossil slabs attached to unsubducted fragments of the Farallon plate. Proc. Natl. Acad. Sci. U. S. A. 110 (14), 5342–5346. https://doi.org/10.1073/pnas.1214880110.

Wang, S., Wang, L., Brown, M., Feng, P., 2016. Multi-stage barite crystallization in partially melted UHP eclogite from the Sulu belt, China. Am. Mineral. 101 (3), 564–579. https://doi.org/10.2138/am-2016-5384.

Wilson, S.A., 1997. The collection, preparing and testing of USGS reference material BCR-2, Columbia River, Basalt, U.S. In: Geological Survey Open-File Report 98-00x.

Wise, W.S., Moller, W.P., 1995. Geology and mineralogy of the New Idria District. Rocks Miner. 70 (1), 30–35. https://doi.org/10.1080/00357529.1995.9926595.

Yamada, C., Tsujimori, T., Chang, Q., Kimura, J.-I., 2019. Boron isotope variations of Franciscan serpentinites, northern California. Lithos 334–335, 180–189. https://doi.org/10.1016/j.lithos.2019.02.004v.